remote sensing

MDPI

Article

A Dark Target Algorithm for the GOSAT TANSO-CAI Sensor in Aerosol Optical Depth Retrieval over Land

Guosheng Zhong [1,*], Xiufeng Wang [2], Meng Guo [3], Hiroshi Tani [2], Anthony R. Chittenden [4], Shuai Yin [1], Zhongyi Sun [1] and Shinji Matsumura [5]

1 Graduate School of Agriculture, Hokkaido University, Sapporo 0608589, Japan; yinshuai@env.agr.hokudai.ac.jp (S.Y.); sunzy025@env.agr.hokudai.ac.jp (Z.S.)
2 Research Faculty of Agriculture, Hokkaido University, Sapporo 0608589, Japan; wang@env.agr.hokudai.ac.jp (X.W.); tani@env.agr.hokudai.ac.jp (H.T.)
3 School of Geographical Sciences, Northeast Normal University, Changchun 130024, China; guom521@nenu.edu.cn
4 Faculty of Fisheries Sciences, Hokkaido University, Hakodate 0418611, Japan; archi@fish.hokudai.ac.jp
5 Faculty of Agriculture, Kagawa University, Sapporo 0608589, Japan; matsu@ag.kagawa-u.ac.jp
* Correspondence: zhgs@env.agr.hokudai.ac.jp; Tel.: +81-11-706-3659

Academic Editors: Alexander A. Kokhanovsky and Prasad S. Thenkabail
Received: 8 February 2017; Accepted: 16 May 2017; Published: 25 May 2017

Abstract: Cloud and Aerosol Imager (CAI) onboard the Greenhouse Gases Observing Satellite (GOSAT) is a multi-band sensor designed to observe and acquire information on clouds and aerosols. In order to retrieve aerosol optical depth (AOD) over land from the CAI sensor, a Dark Target (DT) algorithm for GOSAT CAI was developed based on the strategy of the Moderate Resolution Imaging Spectroradiometer (MODIS) DT algorithm. When retrieving AOD from satellite platforms, determining surface contributions is a major challenge. In the MODIS DT algorithm, surface signals in the visible wavelengths are estimated based on the relationships between visible channels and shortwave infrared (SWIR) near the 2.1 μm channel. However, the CAI only has a 1.6 μm band to cover the SWIR wavelengths. To resolve the difficulties in determining surface reflectance caused by the lack of 2.1 μm band data, we attempted to analyze the relationship between reflectance at 1.6 μm and at 2.1 μm. We did this using the MODIS surface reflectance product and then connecting the reflectances at 1.6 μm and the visible bands based on the empirical relationship between reflectances at 2.1 μm and the visible bands. We found that the reflectance relationship between 1.6 μm and 2.1 μm is typically dependent on the vegetation conditions, and that reflectances at 2.1 μm can be parameterized as a function of 1.6 μm reflectance and the Vegetation Index (VI). Based on our experimental results, an Aerosol Free Vegetation Index ($AFRI_{2.1}$)-based regression function connecting the 1.6 μm and 2.1 μm bands was summarized. Under light aerosol loading (AOD at 0.55 μm < 0.1), the 2.1 μm reflectance derived by our method has an extremely high correlation with the true 2.1 μm reflectance (r-value = 0.928). Similar to the MODIS DT algorithms (Collection 5 and Collection 6), a CAI-applicable approach that uses $AFRI_{2.1}$ and the scattering angle to account for the visible surface signals was proposed. It was then applied to the CAI sensor for AOD retrieval; the retrievals were validated by comparisons with ground-level measurements from Aerosol Robotic Network (AERONET) sites. Validations show that retrievals from the CAI have high agreement with the AERONET measurements, with an r-value of 0.922, and 69.2% of the AOD retrieved data falling within the expected error envelope of $\pm$ (0.1 + 15% $AOD_{AERONET}$).

Keywords: AOD retrieval; dark target algorithm; GOSAT TANSO-CAI; surface reflectance

1. Introduction

Atmospheric aerosols are solid particles or liquid droplets suspended in the atmosphere with diameters ranging from 10^{-3} to 10^{2} micrometers [1]. Aerosol is a major component of the atmosphere and plays an important role in global environmental and climate change [2]. Aerosols can absorb or scatter the incoming solar radiation and affect the Earth's radiation budget, thus modulating the warming or cooling of the Earth [2,3]. Ground-level aerosols, also known as particulate matter (PM), are associated with human health and as such are regulated as a priority air quality pollutant [4,5]. Aerosol monitoring contributes significantly to the understanding of the Earth's environmental systems.

Satellites are increasingly being used to monitor the spatial and temporal distribution of aerosols from a local to global scale, and to study their physical and chemical properties [6]. Spectral aerosol optical depth (AOD) is the most frequently used aerosol optical property, because it is directly related to PM loading. AOD derived from satellite observations has thus been used as a proxy for surface PM [5,7]. AOD is a dimensionless measure of aerosol abundance and the amount of solar light extinction (scattering and absorption) caused by aerosol particles passing through a column of the atmosphere [7,8]. The satellite sensor receives a reflectance containing contributions from both the land surface and the atmosphere (especially aerosols). The main challenge of aerosol retrieval over land is to remove the surface contributions from the integrated reflectance signal at the satellite level [9–11].

Several algorithms have been developed based on different physical principles to separate the surface and atmospheric contributions for different sensors [12]. For instance, Moderate Resolution Imaging Spectroradiometer (MODIS), as typical single-view sensors, use the shortwave infrared (SWIR) channel to determine surface reflectance in the visible (VIS) channels based on the stable relationship between the VIS and SWIR channels [13,14]. Multi-angle Imaging SpectroRadiometer (MISR) and Advanced Along Track Scanning Radiometer (AATSR) are multiangular sensors that make it possible to accurately account for directional surface scattering [15,16]. The Polarization and Directionality of the Earth's Reflectance (POLDER) instrumentation on the Advanced Earth Observing Satellite 1 (ADEOS-1) can achieve polarization measurement, which allows ground contributions to be determined based on the fact that atmospheric scattering is much more polarized than surface reflection [11,17]. Dark Target (DT) is a classic and popular technique for surface reflectance estimation and has been successfully applied to MODIS [18,19], Landsat Thematic Mapper [10], and Advanced Very High Resolution Radiometer (AVHRR) [20,21], as well as several other sensors [22–24]. The DT approach assumes that aerosols over "dark" surfaces (such as vegetated land and dark oceans) will brighten the scene, and the aerosol signal is a major component of the top-of-atmosphere (TOA) signal in this case [24,25]. Thus, low surface reflectance values favor good discrimination between the surface and atmospheric contributions. In the MODIS DT algorithm, the influence of aerosols on the SWIR 2.1 μm channel is negligible (except for heavy aerosol or dusts), so the correlations of reflectance in the 0.47, 0.65, and 2.1 μm channels are used to estimate the surface reflectance. Although highly accurate estimations can be made over low reflectance areas, the DT algorithm is limited by surface conditions and cannot be used over bright-reflection regions, such as cities, deserts, or semi-desert regions; this is because the surface reflectance signals over these regions are too large, which makes it difficult to discriminate aerosol contributions from satellite level TOA signals [1,26,27].

The mature and well-defined MODIS DT algorithm is used to retrieve aerosol properties over the land and ocean twice a day with near-global coverage [12]. In theory, the MODIS DT algorithm can be applied to any sensor that measures reflectance in wavelength bands that cover VIS (red or blue bands) and SWIR (2.1 μm band) [25]. The Dark Target group has already adapted the MODIS DT algorithm to run operationally on the Visible Infrared Imaging Radiometer Suite (VIIRS) instrument aboard the Suomi-NPP polar orbiting satellite so as to create a long-term global AOD record [24,28]. However, it is worth noting that the operational MODIS DT algorithm is based on SWIR-VIS surface relationships, with 2.1 μm being the key band for estimating surface reflectance. As such, adapting the MODIS DT algorithm to the sensors that do not have SWIR bands close the 2.1 μm band is difficult.

The Thermal and Near-Infrared Sensor for Carbon Observation Cloud and Aerosol Imager (TANSO-CAI) is one of the observation instruments onboard the Greenhouse Gases Observing Satellite (GOSAT). The GOSAT was designed to measure the total columns of carbon dioxide and methane, which are observed by the Fourier Transform Spectrometer (TANSO-FTS) [29,30]. The TANSO-CAI visualizes atmospheric and ground surface conditions during the daytime. One of its missions is to detect clouds and aerosols in the FTS's field of view to correct the obtained spectra with FTS [30]. However, because TANSO-CAI is a single-view sensor without any polarization information or SWIR bands near 2.1 μm, most of the conventional aerosol retrieval algorithms are not applicable [31]. For the time being, TANSO-CAI cannot provide any definitive aerosol data, so the aerosol-related information necessary for correcting TANSO-FTS data is derived from other platforms [32]. Although the challenges involved in developing an algorithm for retrieving AOD from GOSAT TANSO-CAI are considerable, such an algorithm is considered essential if precise aerosol information from the TANSO-CAI is ever to be obtained. It has the potential to reduce aerosol-related errors and improve the accuracy of TANSO-FTS data, and will also expand the scope of future aerosol-related research [33].

In this study, we aimed to adapt a MODIS-like DT algorithm to the GOSAT TANSO-CAI, which has only one 1.6 μm SWIR band. Due to the lack of a SWIR band near 2.1 μm, determining the surface reflectance in the VIS band is comparatively difficult [34]. To resolve the difficulty in determining the surface reflectance, we explored the reflectance relationship between the 1.6 μm and 2.1 μm bands (1.6 vs. 2.1), and attempted to develop an operational algorithm for aerosol retrieval.

2. Theoretical Basis of AOD Retrieval

Assuming that the land surface is a Lambertian surface and that the atmospheric and aerosol loading are horizontally uniform, the relationship between TOA reflectance (R_{TOA}), atmospheric contribution (R_{Atm}), and surface reflectance (R_{Surf}) can be described by Equation (1):

$$R_{TOA}(\lambda, \mu_0, \mu, \varphi) = R_{Atm}(\lambda, \mu_0, \mu, \varphi) + \frac{R_{Surf}(\lambda) T_d(\lambda, \mu_0) T_u(\lambda, \mu)}{1 - R_{Surf}(\lambda) S(\lambda)} \quad (1)$$

where λ is a given wavelength; μ_0, μ, and φ are the cosine of the solar zenith angle, the cosine of the satellite zenith angle, and the relative azimuth angle between the sun and the satellite, respectively; S is the atmospheric hemispherical albedo; T_d is the atmospheric transmittance from TOA to the surface; and T_u is the atmospheric transmission from the Earth's surface to a satellite receiver [10,35]. The terms of R_{Atm}, $T_d T_u$, and S are important atmospheric parameters that are functions of the AOD (τ) and can be extracted using the radiative transfer model. Therefore, as Equation (1) shows, if the surface reflectance can be determined, then the AOD can be retrieved. Aerosol retrieval algorithms have been developed for many different satellite platforms based on this principle [36].

The DT approach for estimating surface reflectance over "dark" surfaces has been widely used in aerosol retrieval and atmospheric correction. By using aircraft images from the Landsat Thematic Mapper and the Airborne Visible/Infrared Imaging Spectrometer (AVIRIS), and spectral data measured from the ground, Kaufman et al. [10,37] summarized the linear relationship between the surface reflectance in the blue (0.47 μm) and red (0.65 μm) bands, and reflectance in the 2.1 μm band, as follows:

$$\begin{cases} R_{0.65} = R_{2.1}/2 \\ R_{0.47} = R_{2.1}/4 \end{cases} \quad (2)$$

where $R_{2.1}$ is the reflectance at 2.1 μm. The 2.1 μm band is barely affected by aerosol path radiance and can penetrate most aerosols. Therefore, the surface reflectance in the blue (0.47 μm) and red (0.65 μm) bands can be determined using Equation (2). This method was used to create the MODIS aerosol product of Collection 4. Additional information that allows better estimation of the surface reflectance has recently been introduced into the MODIS DT algorithm. After several studies suggested that the surface reflectance relationships in the VIS and 2.1 μm bands were angle

dependent [38–40], Levy et al. [18] found that different surface types display different ratios between the surface reflectance of the VIS and 2.1 μm bands (the complete regression including slope and y-intercept). To reduce errors in the existing method, Levy et al. expanded Equation (2) and proposed a second-generation operational algorithm for MODIS data (Collection 5), which took the dependencies of angular variability and surface type into account, as in Equations (3):

$$\begin{cases} R_{0.65} = R_{2.1} \times \text{slope}_{0.65/2.1} + \text{yint}_{0.65/2.1} \\ R_{0.47} = R_{0.65} \times \text{slope}_{0.47/0.65} + \text{yint}_{0.47/0.65} \end{cases}$$

where

$$\begin{cases} \text{slope}_{0.65/2.1} = \text{slope}_{0.65/2.1}^{\text{NDVI}_{\text{SWIR}}} + 0.002 \times \Theta - 0.27 \\ \text{yint}_{0.65/2.1} = -0.00025 \times \Theta + 0.033 \end{cases}$$

$$\begin{cases} \text{slope}_{0.47/0.65} = 0.49 \\ \text{yint}_{0.47/0.65} = 0.005 \end{cases}$$

where in turn

$$\begin{cases} \text{slope}_{0.65/2.1}^{\text{NDVI}_{\text{SWIR}}} = 0.48; \ \text{NDVI}_{\text{SWIR}} < 0.25, \\ \text{slope}_{0.65/2.1}^{\text{NDVI}_{\text{SWIR}}} = 0.58; \ \text{NDVI}_{\text{SWIR}} > 0.75, \\ \text{slope}_{0.65/2.1}^{\text{NDVI}_{\text{SWIR}}} = 0.48 + 0.2 \times (\text{NDVI}_{\text{SWIR}} - 0.25); \\ \qquad\qquad 0.25 \leq \text{NDVI}_{\text{SWIR}} \leq 0.75 \end{cases} \quad (3)$$

where $\text{slope}_{0.65/2.1}$ and $\text{yint}_{0.65/2.1}$ are the slope and the intercept for the relationship of the surface reflectance in the 0.65 μm and 2.1 μm channels, and $\text{slope}_{0.47/0.65}$ and $\text{yint}_{0.47/0.65}$ are the slope and intercept for the relationship between the surface reflectance in 0.47 μm and 0.65 μm channels. Θ is the scattering angle, defined as Equation (4). $\text{NDVI}_{\text{SWIR}}$ is an aerosol resistant measure of vegetation "greenness," defined in Equation (5).

$$\Theta = \cos^{-1}(-\cos\theta_0 \cos\theta + \sin\theta_0 \sin\theta \cos\varnothing) \quad (4)$$

where θ_0, θ, and ϕ are the solar zenith angle, the satellite zenith angle, and the relative azimuth angle between the sun and the satellite, respectively.

$$\text{NDVI}_{\text{SWIR}} = (R_{1.2} - R_{2.1})/(R_{1.2} + R_{2.1}) \quad (5)$$

where $R_{1.2}$ is the MODIS-measured reflectance at 1.2 μm. Surface reflectance estimations in both MODIS retrieval algorithm Collection 5 and the currently operational Collection 6 are based on this method.

Due to the lack of any 2.1 μm band on board the GOSAT TANSO-CAI, the MODIS and TANSO-CAI all measure reflectance at 1.6 μm. Note that 1.6 μm and 2.1 μm belong to longer wavelengths that are much less affected by aerosols; thus, if there was a reliable relationship between the reflectance of the 1.6 μm and the 2.1 μm channels, then the potential exists to develop a MODIS-like DT algorithm that uses the 1.6 μm band to estimate VIS surface reflectance.

3. Materials and Methods

3.1. Satellite Data and Ground-Level Data

In this study, TANSO-CAI data from GOSAT, surface reflectance product and aerosol product data from MODIS, and ground-level AOD data from the Aerosol Robotic Network (AERONET) were used.

3.1.1. GOSAT TANSO-CAI Data

The GOSAT satellite is the world's first spacecraft to measure greenhouse gases. A joint project of the Japan Aerospace Exploration Agency (JAXA), the Ministry of the Environment of Japan (MOE), and the National Institute for Environmental Studies (NIES) of Japan, it was successfully launched on 23 January 2009. TANSO-CAI is aboard GOSAT, conducting daytime observations of the atmosphere and ground surfaces in four spectral bands: 1 (0.370–0.390 μm); 2 (0.664–0.684 μm); 3 (0.860–0.880 μm); and 4 (1.560–1.650 μm). The spatial resolution at nadir is 500 m for bands 1–3, and 1500 m for band 4. GOSAT revisits the same point in space every 3 days [30].

GOSAT provides three processing-level products derived from TANSO-CAI observations: radiances, cloud flag, global radiance and reflectance distribution, as well as Normalized Difference Vegetation Index (NDVI) products [30]. In our study, AOD retrieval uses CAI L1B+ radiance products, on which radiometric and geometric corrections (orthorectification, band-to-band registration, and resampling) are performed [41,42]. Before AOD retrieval, the radiance has to be converted to reflectance using Equation (6):

$$R_{TOA} = \left(\pi \times L_\lambda \times d^2\right) / \left(E_\lambda \times \cos\theta_0\right) \quad (6)$$

where L is the radiation brightness of the corresponding TANSO-CAI band, d is the distance between the Sun and the Earth, and E is the solar irradiance with weighting response function of the corresponding TANSO-CAI band. In addition, the CAI L1B+ radiance product provides detailed observational information (such as the solar zenith/azimuth angles and satellite zenith/azimuth angles) [43].

3.1.2. MODIS Surface Reflectance Product (MOD09)

Each MODIS surface reflectance data set (MOD09) is a seven-band product computed from MODIS-Terra Level 1B land bands 1 (0.620–0.670 μm); 2 (0.841–0.876 μm); 3 (0.459–0.479 μm); 4 (0.545–0.565 μm); 5 (1.230–1.250 μm); 6 (1.628–1.652 μm); and 7 (2.105–2.155 μm). After adjusting for the effects of atmospheric gases, aerosols and thin cirrus clouds, the surface reflectance of MOD09 is estimated as if it would have been measured at ground level [44–46]. Thus, MOD09 surface reflectance is the source for the generation of downstream land surface products, such as the Vegetation Index (VI); Leaf Area Index (LAI)/Fraction of Photosynthetically Active Radiation (FPAR); Bidirectional Reflectance Distribution Function (BRDF)/Albedo; Land Cover; Snow Cover; and Thermal Anomalies [47,48]. MOD09 Collection 5 has been validated, and for good quality retrievals (quality assurance: no cloud, cloud shadow, or high aerosol), the accuracy of the 1.6 μm and 2.1 μm channels is such that 97.69% and 98.64% of the observations were within the theoretical error bars of ±(0.005 + 5%) for the responding reflectance band [48].

3.1.3. AERONET AOD Data

The ground-level AOD data are from AERONET [49], a worldwide remote sensing aerosol network that provides information on various aerosol properties using the direct sun measurements of spectral AOD and the use of multiangular and multispectral measurements of sun radiance [2]. Unlike satellite remote sensing, AERONET measurements are unaffected by the uncertainties associated with surface properties and aerosol type assumptions. AERONET AOD products have been validated with a low uncertainty of 0.01 at VIS and near infrared (NIR) wavelengths [49,50]. Thus, AERONET level 2.0 (cloud screened and quality-assured) data were used in this study to validate AOD retrieval from the satellite. In addition, the AERONET data were utilized to assist in the selection of the experimental data. However, since the AOD retrievals in this study were at 0.55 μm, a wavelength that AERONET

does not use to measure AOD, the AERONET AOD needs to be interpolated to 0.55 μm using the Angstrom exponent α [51], defined as,

$$\alpha = -\frac{\ln(\tau_\lambda/\tau_{0.55})}{\ln(\lambda/0.55)} \quad (7)$$

3.2. The Relationship between Reflectances at 1.6 μm and 2.1 μm

To analyze the reflectance relationship of 1.6 vs. 2.1, the MODIS surface reflectance product was used as the experimental data. Knowledge of AOD is an important factor that can affect the accuracy of the surface reflectance product [52,53]. As such, the experimental data selection referenced ground-level AOD measurements taken from close proximity to the AERONET sites to ensure the data used in the analyses were highly accurate. The experimental surface reflectance data were selected from nine AERONET sites in different global regions according to the following criteria: the MOD09 data should be obtained under cloud-free conditions, from locations within 25 km from the AERONET sites; the MODIS-Terra overpasses within ±30 min of the AERONET measurements; and the measured AOD values should be lower than 0.1 (in order to minimize the influence of multiple aerosol scattering).

The linear relationship of surface reflectances at 1.6 μm and 2.1 μm is shown in Figure 1a, and has a correlation coefficient (r) value of 0.847. Despite the high r-value, the relationship of 1.6 vs. 2.1 shows considerable scatter. For example, when the surface reflectance value of the 1.6 μm channel is 0.2, the corresponding scatter plots show surface reflectance values of the 2.1 μm channel ranging from 0.055 to 0.175, obviously biased against the regression line. Such uncertainty could result in incorrect surface reflectance estimations, thereby leading to large errors in AOD retrieval [18].

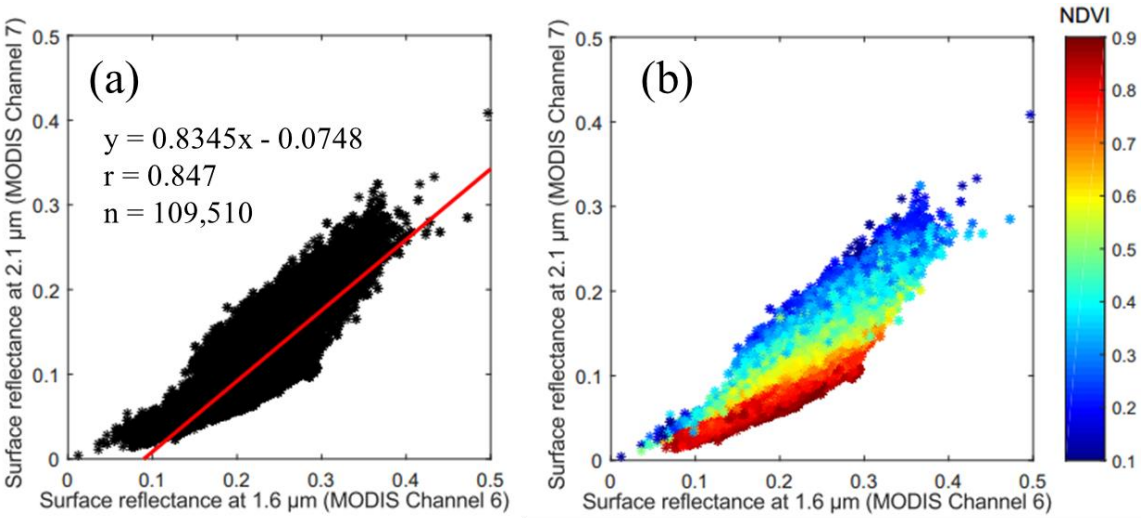

Figure 1. Scatter plots between Moderate Resolution Imaging Spectroradiometer (MODIS) surface reflectances at 1.6 μm and 2.1 μm. (**a**) The spectral linear relationship of surface reflectances at 1.6 μm and 2.1 μm; (**b**) Surface reflectances at 2.1 μm as a function of surface reflectance at 1.6 μm and the Normalized Difference Vegetation Index (NDVI). The color bar shows the NDVI values for each point.

In light of this, the relationship between the surface reflectance at 0.6 μm and 2.1 μm is more robust, while the relationship between the surface reflectance at 0.6 μm and 1.6 μm is very sensitive to the amount of surface vegetation [18,22,54]. It could be expected that the surface reflectance relationship of 1.6 vs. 2.1 may also be dependent on the amount of vegetation. To confirm this conjecture and to develop a method for reducing scatter in the relationship between 1.6 vs. 2.1, we used the NDVI as a tuner to explore a new relationship. The NDVI is a commonly applied numerical indicator used for evaluating vegetation conditions; it could be calculated with the reflectance of the red and NIR

bands obtained from the space platform using Equation (8) [55]. NDVI values range from negative one to positive one; zero and negative values represent non-vegetated surfaces (such as soil, water, and snow), and higher values indicate the higher possible densities of green vegetation [56].

$$\mathrm{NDVI} = (\mathrm{R_{NIR}} - \mathrm{R_{red}})/(\mathrm{R_{NIR}} + \mathrm{R_{red}}) \quad (8)$$

where $\mathrm{R_{NIR}}$ and $\mathrm{R_{red}}$ are the reflectances of the NIR and red bands, respectively.

Figure 1b shows the relationship between surface reflectances at 1.6 μm and 2.1 μm. The colors of the points are their corresponding NDVI values, according to the colored bar. As the figure shows, the NDVI is a significant factor in the relationship of 1.6 vs. 2.1. The exhibited evident regulation according to NDVI distribution is that the relationship of 1.6 vs. 2.1 seems to be vegetation dependent. As NDVI values vary from high to low, the slope of the corresponding linear relationship of 1.6 vs. 2.1 is continuously increasing. This verifies the previous conjecture that the relationship of 1.6 vs. 2.1 is also sensitive to the amount of vegetation.

Compared with using the linear relationship of 1.6 vs. 2.1 directly, as shown in Figure 1a, it is possible to improve the accuracy of surface reflectance estimation through an NDVI-based correlation of 1.6 vs. 2.1. However, it is important to note that aerosols can influence the NDVI, with NDVI values typically decreasing as AOD increases, thus limiting its potential to evaluate surface conditions [1,22]. To overcome this drawback, other vegetation indices that are not sensitive to atmospheric aerosols could replace the NDVI. In the Dark Target algorithm Collection 5 and Collection 6, the $\mathrm{NDVI_{SWIR}}$, a measure of vegetation "greenness" highly correlated with the regular NDVI, was proposed. $\mathrm{NDVI_{SWIR}}$ (shown as Equation (5)) is defined as a function of the MODIS-measured reflectances of the 1.2 μm and 2.1 μm channels. Because longer wavelengths are much less affected by aerosols, consequently, $\mathrm{NDVI_{SWIR}}$ is aerosol resistant [18,57].

GOSAT TANSO-CAI does not possess the 1.2 μm and 2.1 μm bands, making it difficult to apply $\mathrm{NDVI_{SWIR}}$ in this instance. We attempted to employ the Aerosol Free Vegetation Index ($\mathrm{AFRI_{2.1}}$) [58] to establish a new VI-based relationship for 1.6 vs. 2.1. $\mathrm{AFRI_{2.1}}$ is calculated by using the NIR and SWIR bands as follows:

$$\mathrm{AFRI_{2.1}} = (\mathrm{R_{NIR}} - 0.5 \times \mathrm{R_{2.1}})/(\mathrm{R_{NIR}} + 0.5 \times \mathrm{R_{2.1}}) \quad (9)$$

where $\mathrm{R_{NIR}}$ is the reflectance of the NIR (MODIS channel 2). In this equation, the coefficient 0.5 is determined based on the experiment results of Karnieli et al. [58], who flew over a variety of ground surfaces in Israel, and performed measurements using a field spectrometer under clear sky conditions. The empirical linear relationship between the SWIR spectral band around 2.1 μm and the red band around 0.6 μm was revealed as $\mathrm{R_{0.6}} = 0.5\mathrm{R_{2.1}}$. One key difference that emerges when comparing $\mathrm{AFRI_{2.1}}$ (Equation (9)) with the regular NDVI (Equation (8)), is that the reflectance of the red band in the NDVI has been replaced by the reflectance of the SWIR (2.1 μm) band, according to the mathematical relationship between the red and SWIR (2.1 μm) bands. Because the wavelength of SWIR is considered to have a much longer wavelength than most aerosols, SWIR has the ability to penetrate atmospheric aerosols. In addition, SWIR is sensitive to vegetation. With these advantages, $\mathrm{AFRI_{2.1}}$ is less susceptible to aerosol influence [58–60].

We used the $\mathrm{AFRI_{2.1}}$ to interpret how the relationship of 1.6 vs. 2.1 changes with different surface conditions. The results are displayed in Figure 2, which also shows similarities to Figure 1b. To study in more quantitative detail how the relationship of 1.6 vs. 2.1 varies with $\mathrm{AFRI_{2.1}}$, we picked out and grouped several experimental data from the sum of points in Figure 2, according to certain given $\mathrm{AFRI_{2.1}}$ values. Each of the selected points groups is displayed in Figure 3, in which the surface reflectance of the 2.1 μm band is a function of the surface reflectance at 1.6 μm and the given $\mathrm{AFRI_{2.1}}$ values. The given $\mathrm{AFRI_{2.1}}$ values are all from 0.400 to 0.900, with intervals of 0.05. Compared with the linear correlation of 1.6 vs. 2.1 (in Figure 1a), all the scatter plots in Figure 3 have stronger correlations, and their corresponding r-values are seemingly higher than that in Figure 1a, implying that such an

$AFRI_{2.1}$-based relationship has the potential capacity to describe the relationship of 1.6 vs. 2.1 with higher accuracy than merely using the general linear relationship (as shown in Figure 1a). Considering the regression functions of these scatter plots in Figure 3, the slopes of their regression lines become distinctly smaller as their $AFRI_{2.1}$ values increase. In order to understand the changes of these regression functions with varied $AFRI_{2.1}$, the slopes and intercepts of these regression lines were compared with their corresponding $AFRI_{2.1}$ values. Figure 4 shows that there is a very strong inverse relationship between the slope and $AFRI_{2.1}$, and its r-value is as high as -0.968. In addition, the relationship between intercepts and $AFRI_{2.1}$ has an r-value of -0.742. Based on these results, the slope and intercept for the relationship of 1.6 vs. 2.1 for different $AFRI_{2.1}$ values can be determined, allowing an $AFRI_{2.1}$-based regression function (Equation (10)) for estimating the reflectance in the 2.1 µm channel from the 1.6 µm channel to be formulated as follows:

$$R_{2.1} = Slope_{1.6/2.1} \times R_{1.6} + Intercept_{1.6/2.1}$$

with

$$\begin{aligned} Slope_{1.6/2.1} &= a_1 \times AFRI_{2.1} + b_1 \\ Intercept_{1.6/2.1} &= a_2 \times AFRI_{2.1} + b_2 \end{aligned} \quad (10)$$

where $R_{2.1}$ and $R_{1.6}$ are the surface reflectances at 2.1 µm and 1.6 µm, and $Slope_{1.6/2.1}$ and $Intercept_{1.6/2.1}$ are the function of $AFRI_{2.1}$, with the coefficients $a_1 = -0.7606$, $b_1 = 0.9763$, $a_2 = -0.0332$, and $b_2 = 0.0286$, which are decided according to the experiment results in Figure 4. We tested the performances of the linear regression function (as shown in Figure 1a) and the $AFRI_{2.1}$-based regression function derived by our team. The estimated results using the linear and the $AFRI_{2.1}$-based regression functions are compared with the true values, and the results are shown in Figure 5a,b, respectively. It is obvious that the $AFRI_{2.1}$-based estimations correlate better with the true values. The comparisons in Figure 5b show much less scattering, and the r-value of the regression has clearly improved.

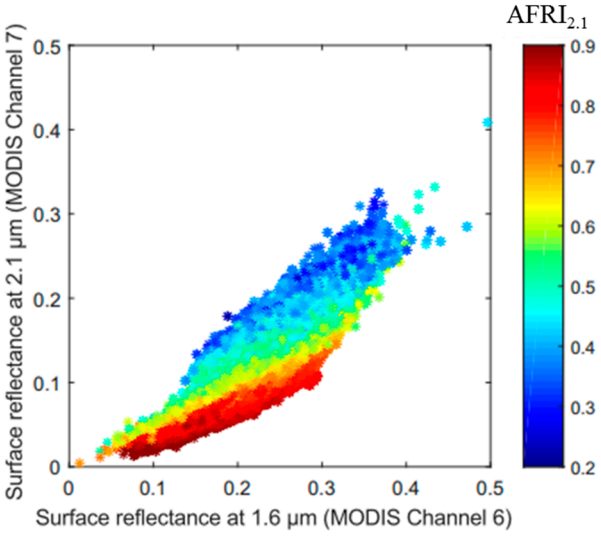

Figure 2. The MODIS surface reflectances at 2.1 µm as a function of surface reflectance at 1.6 µm and $AFRI_{2.1}$. The color bar shows the values of $AFRI_{2.1}$ for each point.

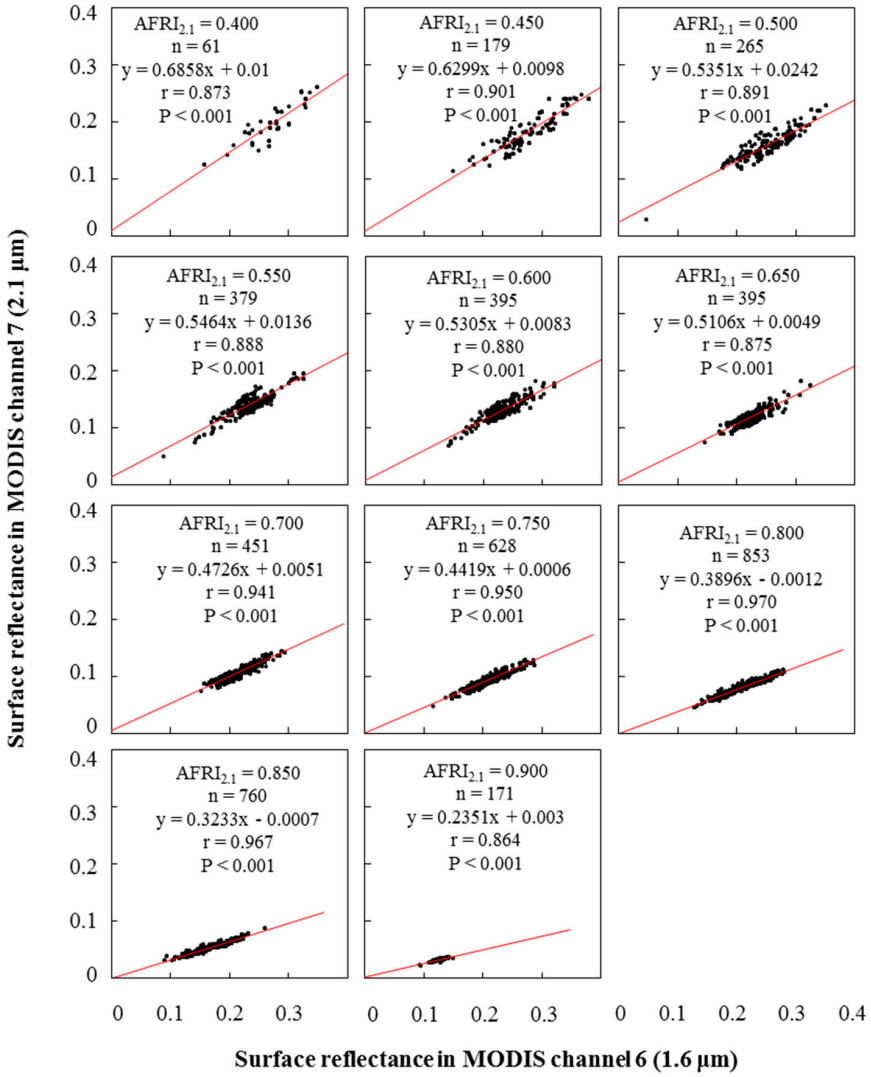

Figure 3. The relationship between surface reflectances at 2.1 µm and 1.6 µm vary with different Aerosol Free Vegetation Index ($AFRI_{2.1}$) values. (All data points in each graph fall within the $AFRI_{2.1}$ value ± 0.001).

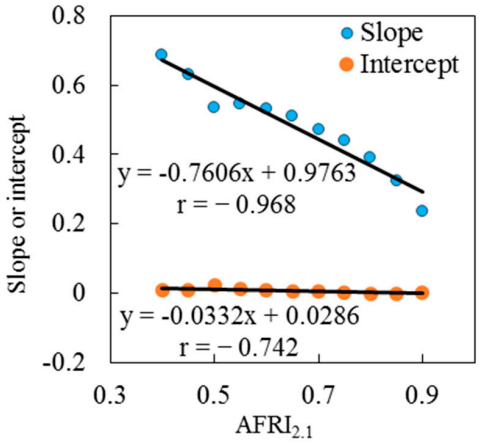

Figure 4. The slopes and intercepts of regression functions (for each graph in Figure 3) as a function of $AFRI_{2.1}$.

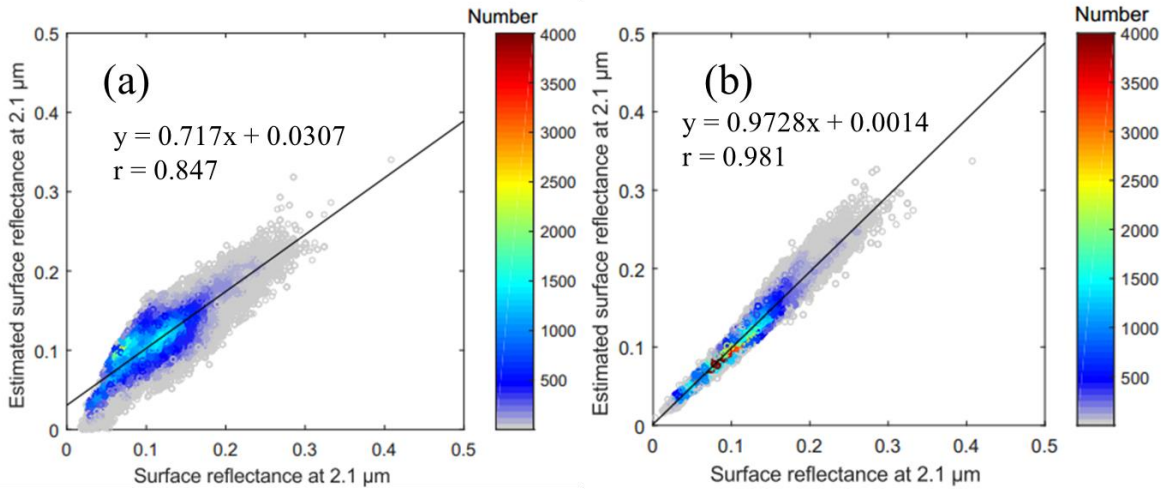

Figure 5. Comparisons of the estimated and the true surface reflectance at 2.1 μm. (**a**) The estimated surface reflectance is derived using the linear relationship shown in Figure 1a; (**b**) The estimated surface reflectance is derived from the known $AFRI_{2.1}$ using the $AFRI_{2.1}$-based regression function (Equation (10)). The color bar shows the number for each point.

3.3. Estimation of Aerosol Free Vegetation Index ($AFRI_{2.1}$) Using NIR and 1.6 μm Bands

Although the $AFRI_{2.1}$-based approach performed well in testing, it is worth noting that the test results shown in Figure 5b are based on known $AFRI_{2.1}$. For sensors equipped with 2.1 μm and NIR bands, the $AFRI_{2.1}$ can easily be directly calculated using Equation (9). However, it is not feasible to derive the $AFRI_{2.1}$ from unequipped sensors (e.g., GOSAT TANSO-CAI). To resolve this difficulty, we developed a new method to estimate $AFRI_{2.1}$ using the 1.6 μm band. Equations (9) and (10) can be rewritten as Equations (11) and (12):

$$AFRI_{2.1} = (R_{0.8} - 0.5 \times R_{2.1})/(R_{0.8} + 0.5 \times R_{2.1}) \quad (11)$$

$$R_{2.1} = (a_1 \times AFRI_{2.1} + b_1) \times R_{1.6} + a_2 \times AFRI_{2.1} + b_2 \quad (12)$$

where $R_{0.8}$ is the reflectance of the MODIS NIR channel, of which the center wavelength is at 0.86 μm. To substitute Equation (12) into Equation (11), the unknown term $R_{2.1}$ can be eliminated; after rearranging, a quadratic equation in $AFRI_{2.1}$ can be obtained (Equation (13)). The solutions are presented as Equation (14):

$$AFRI_{2.1}^2 \times 0.5 \times (a_1 \times R_{1.6} + a_2) + AFRI_{2.1} \times (R_{0.8} + 0.5 \times (a_1 + b_1) \times R_{1.6} + 0.5 \times (a_2 + b_2)) + (0.5 \times b_1 \times R_{1.6} + 0.5 \times b_2 - R_{0.8}) = 0 \quad (13)$$

$$AFRI_{2.1} = \frac{-(R_{0.8} + 0.5 \times (a_1 + b_1) \times R_{1.6} + 0.5 \times (a_2 + b_2)) \pm \sqrt{(R_{0.8} + 0.5 \times (a_1 + b_1) \times R_{1.6} + 0.5 \times (a_2 + b_2))^2 - 4 \times 0.5 \times (a_1 \times R_{1.6} + a_2) \times (0.5 \times b_1 \times R_{1.6} + 0.5 \times b_2 - R_{0.8})}}{2 \times 0.5 \times (a_1 \times R_{1.6} + a_2)} \quad (14)$$

$AFRI_{2.1}$ in Equations (13) and (14) can be estimated using the 0.8 μm and 1.6 μm bands. In actual application, $AFRI_{2.1}$ solutions have two roots, because the $AFRI_{2.1}$ values should all be within the range of −1 to 1 (similar to the NDVI); thus, there would be one reasonable root falling inside this range, with another unreasonable root falling outside of it. Using the estimated $AFRI_{2.1}$ and Equation (12), the $R_{2.1}$ can be calculated. The performances of the $AFRI_{2.1}$ and $R_{2.1}$ values estimated using the 1.6 μm-based approach were also tested by comparing them with their corresponding true values. Figure 6a shows the scatter plot of the estimated $AFRI_{2.1}$ versus true $AFRI_{2.1}$, and Figure 6b shows the scatter plot of the estimated $R_{2.1}$ versus the true $R_{2.1}$. All estimations show very good agreement with the true values, and the derived r-values are all above 0.92. The regression slope value is near to 1, and the intercept is close to 0.

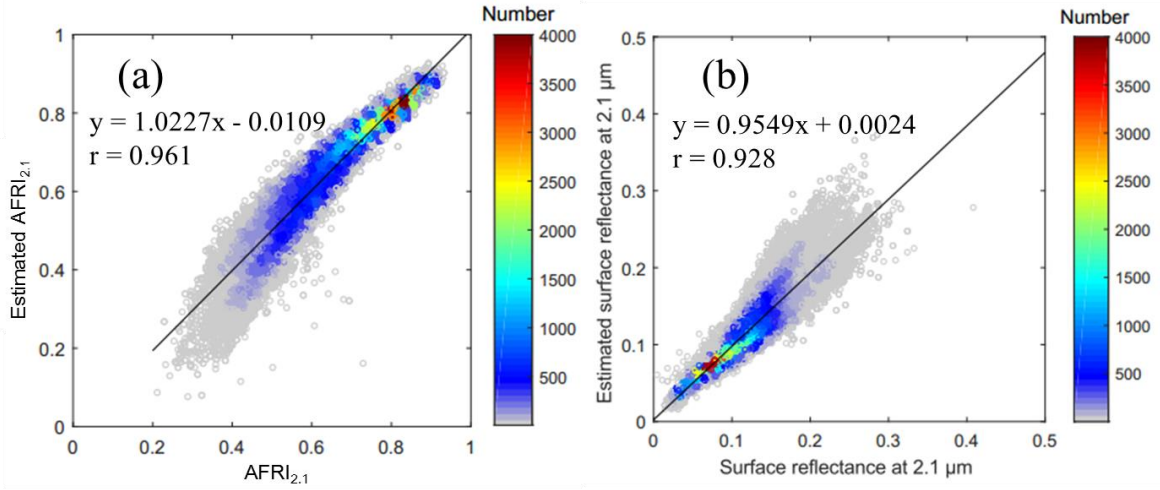

Figure 6. Comparisons of the estimated results and the true values. (**a**) Comparisons of the estimated $AFRI_{2.1}$ and the true $AFRI_{2.1}$; (**b**) Comparisons of the estimated and the true surface reflectance at 2.1 μm. The estimated surface reflectance at 2.1 μm is from the $AFRI_{2.1}$ estimated using the proposed method (Equations (11)–(14)). The color bars show the number for each point.

3.4. Estimation of TANSO-CAI Surface Reflectance at 0.67 μm from the 1.6 μm Band

An $AFRI_{2.1}$-based regression function used to describe the reflectance relationship of 1.6 vs. 2.1 was established through experimentation with MODIS surface reflectance products. Following the method used in the MODIS DT algorithm, the surface reflectance for the 0.6 μm band can be obtained from the 1.6 μm band by using the estimated reflectance at 2.1 μm. In the operational MODIS DT algorithm version of Collection 5 and the current Collection 6, the reflectance relationship of the 0.6 μm and 2.1 μm bands is adjusted according to geometry and vegetation amount. The geometry is based on the scattering angle (Equation (4)), and the vegetation amount is estimated by $NDVI_{SWIR}$ (Equation (5)), a variant of the NDVI based on the SWIR bands [61]. When developing a MODIS-like AOD retrieval algorithm for TANSO-CAI, the scattering angle can be easily determined using observational information such as the solar zenith/azimuth angle and the satellite zenith/azimuth angle. $AFRI_{2.1}$ can also accurately predict the vegetation amount. The relationship between $NDVI_{SWIR}$ and $AFRI_{2.1}$ was calculated using experimental MODIS surface products, and is presented in Figure 7. It is evident that $AFRI_{2.1}$ correlates highly with $NDVI_{SWIR}$ (r = 0.943). According to this relationship, $AFRI_{2.1}$ can be considered an appropriate replacement for $NDVI_{SWIR}$ and suitable for practical use in the surface reflectance estimation method. Based on the previous analysis, a 1.6 μm band-based method that follows the MODIS DT algorithm (Equations (3)) for estimating surface reflectance at 0.6 μm can be described as follows:

$$R_{0.6} = R_{2.1}^{\text{Estimated}} \times \text{slope}_{0.6/2.1} + \text{yint}_{0.6/2.1}$$

where

$$\begin{cases} \text{slope}_{0.6/2.1} = \text{slope}_{0.6/2.1}^{AFRI_{2.1}} + 0.002 \times \Theta - 0.27 \\ \text{yint}_{0.6/2.1} = -0.00025 \times \Theta + 0.033 \end{cases}$$

where in turn

$$\begin{cases} \text{slope}_{0.6/2.1}^{AFRI_{2.1}} = 0.48;\ AFRI_{2.1} < 0.46, \\ \text{slope}_{0.6/2.1}^{AFRI_{2.1}} = 0.58;\ AFRI_{2.1} > 0.89, \\ \text{slope}_{0.6/2.1}^{AFRI_{2.1}} = 0.48 + 0.2 \times (1.154 \times AFRI_{2.1} - 0.531); \\ \qquad\qquad 0.46 \le AFRI_{2.1} \le 0.89 \end{cases} \quad (15)$$

where the $AFRI_{2.1}$ and the estimated reflectance at 2.1 μm, $R_{2.1}^{Estimated}$ can all be determined using the 1.6 μm band, according to the method described in Section 3.3.

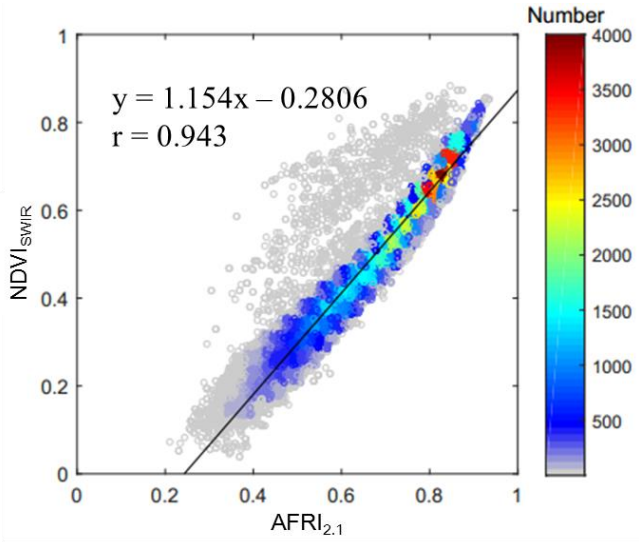

Figure 7. The relationship between $NDVI_{SWIR}$ and $AFRI_{2.1}$. Both $NDVI_{SWIR}$ and $AFRI_{2.1}$ are calculated using MODIS surface reflectance products. The color bar shows the number for each point.

Table 1 summarizes the specifications of the MODIS and GOSAT TANSO-CAI bands associated with this study. Although both GOSAT TANSO-CAI and MODIS have bands near the 0.6 μm, 0.8 μm, and 1.6 μm wavelengths, differences exist in their center wavelengths and bandwidths, as well as in their spectral response functions. When applying Equations (15) to GOSAT TANSO-CAI data, the differences between the two platforms should first be determined and then corrected. Moreover, because the proposed method was developed based on MODIS experimental data, it should be noted that in actual application the surface reflectance of 0.6 μm would be estimated from the TOA reflectances of the 0.8 μm and 1.6 μm bands. In order to adapt the method (shown as Equations (15)) that was developed based on the MODIS data to TANSO-CAI, we compared the uncorrected surface reflectance generated by directly applying Equations (15) to the TANSO-CAI data against the theoretical surface reflectance. An empirical function for correcting platform differences was summarized as:

$$R_{0.67}^{Corrected} = 1.2 \times R_{0.67}^{Uncorrected} + 0.015 \quad (16)$$

where $R_{0.67}^{Corrected}$ is the corrected surface reflectance in the TANSO-CAI 0.67 μm band, and $R_{0.67}^{Uncorrected}$ is the uncorrected surface reflectance. Here, the theoretical surface reflectance is derived by the atmospheric correction with help from a Second Simulation of a Satellite Signal in the Solar Spectrum (6S) radiative transfer code [62], and the spatially and temporally matched AERONET data. Atmospheric correction is an important step to negate the atmospheric effects and derive surface reflectance values from satellite-observed data [18,63]. The 6S code is a physically based model and offers the atmospheric correction working modality to compute the surface reflectance [64]. For atmospheric correction, we selected spatially and temporally matched TANSO-CAI/AERONET collocated data according to the following criteria: AERONET sites measured within 30 min of the GOSAT overpasses, and the selected TANSO-CAI data were located within a 25 km radius around the AERONET sites. In addition, to ensure the accuracy of atmospheric correction and to avoid influence from multiple aerosol scattering, the selected collocated data for atmospheric correction should have a low AOD value ($\tau_{0.55} < 0.1$).

Table 1. Parameters of the corresponding Greenhouse Gases Observing Satellite Thermal and Near-Infrared Sensor for Carbon Observation Cloud and Aerosol Imager (GOSAT TANSO-CAI) and MODIS bands used in this study.

GOSAT TANSO-CAI				MODIS			
Band Number	Central Wavelength (μm)	Bandwidth (μm)	Spatial Resolution (m)	Band Number	Central Wavelength (μm)	Bandwidth (μm)	Spatial Resolution (m)
2	0.674	0.664–0.684	500	1	0.645	0.620–0.670	250
3	0.870	0.860–0.880	500	2	0.859	0.841–0.876	250
4	1.600	1.560–1.650	1500	6	1.640	1.628–1.652	500
				7	2.130	2.105–2.155	500

3.5. AOD Retrieval

The flowchart for GOSAT TANSO-CAI AOD retrieval is illustrated in Figure 8. The surface contributions can be determined using the methods mentioned previously. We can derive the AOD by solving Equation (1) using the following atmospheric parameters (R_{Path}, T_dT_u, and S). As solving the equation is a time-consuming process, a look-up table method based on a large range of pre-computed atmospheric parameters using corresponding pre-set geometrical conditions (θ_0, θ, and ϕ) and AOD values was prepared to improve the efficiency of the AOD retrieval procedure. The atmospheric parameters (R_{Path}, T_dT_u, and S) can be pre-computed by repeatedly running the 6S radiative transfer code with different parameter combination inputs. The 6S radiative transfer code requires the following parameters as the input: spectral conditions, geometrical conditions, atmospheric model, aerosol model type, and AOD values. In the look-up table, the input parameters of the 6S radiative transfer code for pre-computing the atmospheric parameters (R_{Path}, T_dT_u, and S) are shown in Table 2. For the GOSAT TANSO-CAI band 2, twenty-one solar zenith angles, six satellite zenith angles, and nine relative azimuth angles were pre-set to describe different geometrical conditions. Three different atmospheric models (Tropical, Midlatitude Summer, and Midlatitude Winter) were taken into account. The continental aerosol model, a broadly used assumption for over land retrieval, was selected as the aerosol model. AOD values were set from 0.01 to 2.00, with intervals of 0.01, and the smallest value was set as 0.001.

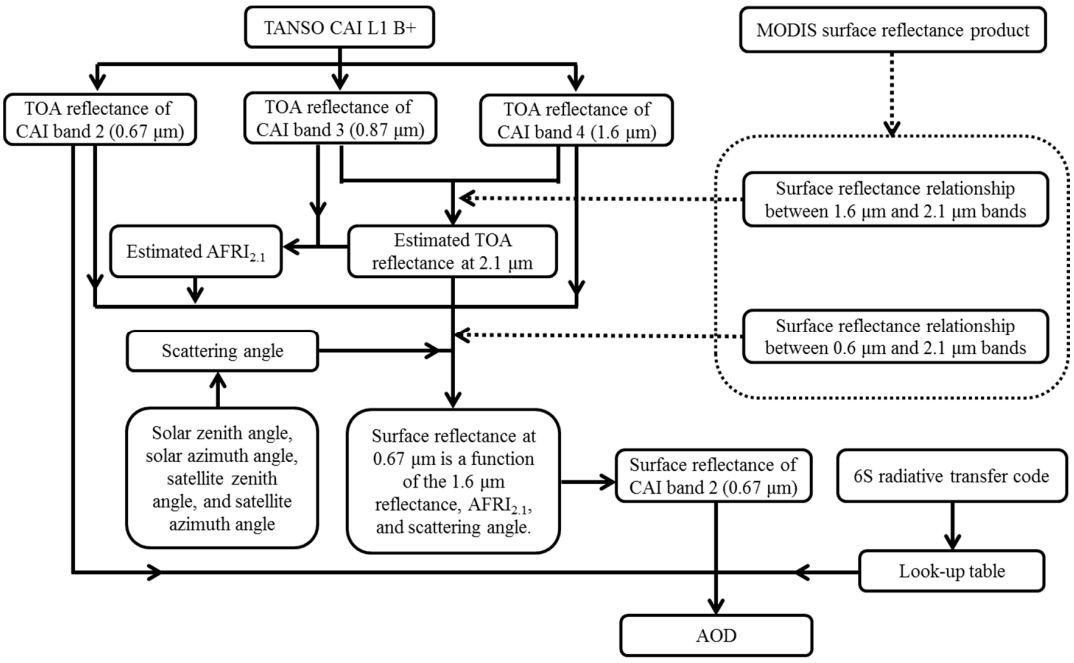

Figure 8. Flow chart of the GOSAT TANSO-CAI retrieval procedure. Dashed lines indicate the analysis of the relationship between associated bands using MODIS surface reflectance products.

Table 2. The input parameters of the 6S radiation transfer code for a pre-computing look-up table.

Parameters	Values
Spectral band	GOSAT TANSO-CAI band 2 (central wavelength at 0.67 μm)
Solar zenith angle	From 0° to 60°, with a step of 3°
Satellite zenith angle	From 0° to 60°, with a step of 12°
Relative azimuth angle	From 0° to 168°, with a step of 24°; and 180°
Atmospheric model	Midlatitude Summer, Midlatitude Winter, and Tropical
Aerosol models	Continental aerosol model
AOD at 0.55 μm	Smallest with a value of 0.001, and from 0.01 to 2.00, with a step of 0.01

When using this look-up table to retrieve AOD for satellite data, the pre-set solar zenith angle, satellite zenith angle and relative azimuth angle combination closest to the actual satellite observation would be sought. Under the targeted geometrical condition, there are multiple corresponding sets of atmospheric parameters (R_{Path}, T_dT_u, and S) that have been pre-computed and recorded according to the different pre-set AOD values. Substituting every set of atmospheric parameters (R_{Path}, T_dT_u, and S) and the estimated surface reflectance into Equation (1) in sequence allows the theoretical TOA reflectance for each sequence to be calculated. In the calculated multiple theoretical TOA reflectance, the value that is closest to the actual TOA reflectance would be selected, and the AOD value of this selected set would be considered as the retrieved AOD.

In the actual retrieval, however, not all the pixels meet the requirements of the retrieval algorithm; to ensure retrieval accuracy, only the well-suited pixels should be taken into account during the retrieval. For example, it is possible to derive the AOD for pixels that have $AFRI_{2.1}$ values less than 0.4. Our algorithm, however, works best when the $AFRI_{2.1}$ values are within the range of 0.4–0.9 (as shown in Figure 4). Therefore, when the $AFRI_{2.1}$ values of pixels were outside this range, then errors in surface reflectance assumptions would increase, and the accuracy of the results would decrease. Additionally, regarding the limitations of the instrumentation, because the sensor receives TOA reflectance at certain wavelengths, values are variable with respect to the surface contributions, aerosol loading, and geometrical conditions (solar zenith angle, satellite zenith angle, and relative azimuth angle). In order to explore the application limitations of the TANSO-CAI band 2 in AOD retrieval, we simulated how TOA reflectance changes with different surface reflectances and different AOD values. The simulation was conducted with 10 different geometrical condition combinations (shown in Table 3) and five different AOD values ($\tau_{0.55}$ = 0.1, 0.5, 1.0, 1.5, and 2.0). Figure 9a–j show the simulation results according to the geometrical conditions cases of a–j in Table 3. Except for Figure 9j, which was simulated under extremely special geometrical conditions, all of the other sub-figures demonstrated that a lower surface reflectance has larger amplitudes of variation in TOA reflectance, with the AOD increasing. This indicated that when using TANSO-CAI band 2 in AOD retrieval, ground surfaces that have a lower surface reflectance are more sensitive to AOD changes. Based on the experimental results, two thresholds have been set for selecting well-suited pixels in the retrieval scheme: the upper limit of surface reflectance in TANSO-CAI band 2 is set to 0.085 and, at the same time, the TOA reflectance of band 3 should be larger than 0.225.

Table 3. Description of the set of different geometrical conditions used to simulate the relationship between TANSO-CAI TOA reflectance and AOD with different surface conditions.

Case Name	Solar Zenith (Degree)	Satellite Zenith (Degree)	Relative Azimuth (Degree)
a	30	0	0
b	30	30	0
c	30	30	180
d	30	60	0
e	30	60	180
f	60	0	0
g	60	30	0
h	60	30	180
i	60	60	0
j	60	60	180

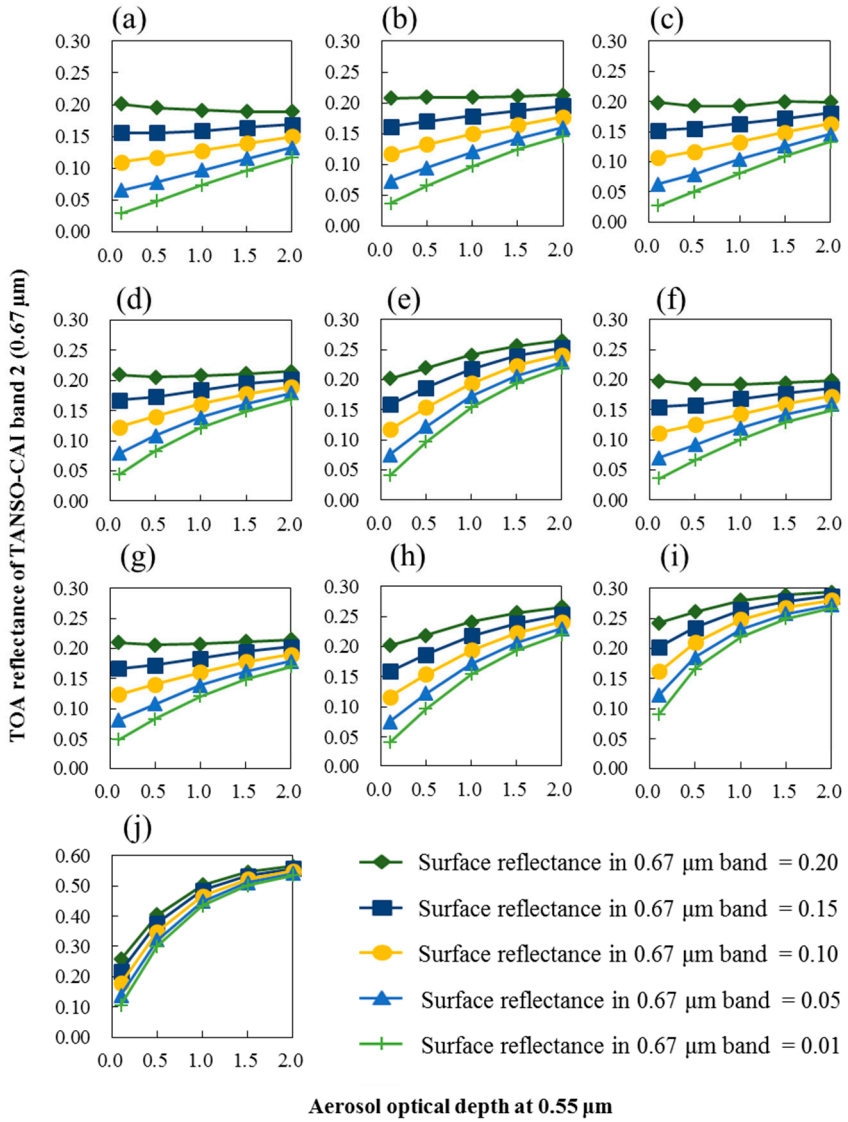

Figure 9. GOSAT TANO-CAI top-of-atmosphere (TOA) reflectance at 0.67 µm as a function of aerosol optical depth (AOD) under different surface reflectances; (**a**–**j**) are simulated under the corresponding observation geometric conditions cases of (**a**–**j**) shown in Table 3.

4. Results and Discussion

The performance of TANSO-CAI retrieval AOD values at 0.55 μm with our algorithm has been evaluated by comparison with ground-level measurements from the collocated AERONET. As the AERONET AOD product has very high accuracy, it is usually considered as "ground truth" and is widely used for the quantitative validation of satellite-based retrievals [65]. To ensure comparability between the ground and satellite levels, spatially and temporally collocated TANSO-CAI and AERONET data were chosen based on the following criteria: the AERONET measurements are conducted within ±15 min of the GOSAT overpass time, and the TANSO-CAI data are collected within a 10-kilometer radius circular validation area around the AERONET site.

In this study, a total of 117 TANSO-CAI and AERONET collocated data were selected from five AERONET sites (Vientiane, Xinglong, Dhaka_University, Chiang_Mai_Met_Sta, and Ussuriysk) during the period from April 2009 to August 2014. The geographical information (longitude, latitude, and elevation) of these AERONET sites is shown in Table 4. Both the Vientiane and Chiang_Mai_Met_Sta sites are located in Southeast Asia, and the Dhaka_University, Xinglong, and Ussuriysk sites are located in South Asia, East Asia, and North Asia, respectively. Figure 10 illustrates the variations of matched TANSO-CAI and AERONET AODs, with observation dates for these five sites. Figure 11 shows the scatter plots between the TANSO-CAI AOD and AERONET AOD for individual and entire sites, and their corresponding summary statistics: the number of samples (N), mean AERONET AOD, root mean square error (RMSE), mean bias error (MBE), and expected error (EE) are shown in Table 4. As Figure 10 shows, the behavior of AODs from TANSO-CAI and AERONET is generally consistent for each site. In this regard, the retrievals are correlated with the overall AERONET sites, with r-values larger than 0.791. Even so, individual regions have their own particular characteristics. Apparently, the AODs retrieved from TANSO-CAI are slightly lower than the AERONET measurements over the Xinglong (Figure 10b) and Ussuriysk sites (Figure 10e), but conversely, the AODs retrieved over the Dhaka_University site (Figure 10c) are generally higher than the AERONET AODs. We could note that the AOD measurement data from the Xinglong and Ussuriysk sites are very low, with mean AOD values of 0.164 and 0.249, respectively. In addition, the dominant land cover type within a 10-km radius around these two sites is tree cover—broadleaved and deciduous [66]. Similarly, the studies of Xie et al. [67] show that, for vegetated sites under low aerosol AOD conditions, the MODIS DT tends to be underestimated. It could be due to an intrinsic system error in the algorithm or an instrument calibration issue. Alternately, the dominant land cover type around the Dhaka_University site is urban, with urban areas comprising approximately 60% of the area within the 10-kilometer radius around the site [66]. Due to the complexity of urban type surfaces, this incorrect estimation of surface reflectance may impact the retrieval quality. On the other hand, the aerosol model assumption is also a critical factor closely associated with the retrieval results. The AOD over the Dhaka_University site is very high, with a mean value of 0.915. As Figure 10c shows, largely overestimated retrievals frequently occurred during the period from February to April for two consecutive years (2013 and 2014). This is possibly because the aerosol assumption cannot reflect the characteristics of atmospheric aerosols during this period. For these reasons, the retrievals over this site have the highest RMSE (0.328) and MBE (0.245). Very high correlation and low error rates are observed over the Vientiane (r-value = 0.921, RMSE = 0.141, and MBE = −0.059) and Chiang_Mai_Met_Sta (r-value = 0.974, RMSE = 0.140, and MBE = 0.099) sites, which are under a high level of aerosol loading and have a mean AERONET AOD of more than 0.7 and 0.5, respectively. The high quality of retrieval is possibly due to the rural vegetated land cover type around the sites [68].

The regression equations and lines of the TANSO-CAI versus AERONET AODs are displayed in Figure 11. In addition, the dashed lines in the graphs are the EE lines. The EE is a confidence envelope that quotes the sum of the absolute and relative AOD errors, and is often used to estimate the uncertainty of aerosol products, such as the MODIS aerosol products. When 66% (one standard deviation) of the points fall within a bounding envelope of the EE as compared to AERONET, the products are considered "validated." For the MODIS DT product (Collection 5 and Collection 6), the

EE for the land AOD product is $\pm(0.05 + 0.15\tau)$, where τ is the true AOD value [69,70]. The envelope of the EE as described in Equation (17) shows:

$$\mathrm{AOD}_{\mathrm{AERONET}} - |\mathrm{EE}| \leq \mathrm{AOD}_{\mathrm{TANSO-CAI}} \leq \mathrm{AOD}_{\mathrm{AERONET}} + |\mathrm{EE}| \quad (17)$$

In Table 4, two different EEs (EE1: $\pm(0.05 + 0.15\tau)$ and EE2: $\pm(0.1 + 0.15\tau)$) have been tentatively defined to estimate the uncertainty values of our algorithm. According to our statistical analysis, only the retrievals over Vientiane were "validated" by the EE1 criterion, with 78.6% of match-ups falling within the EE envelope of $\pm(0.05 + 0.15\tau)$. For the total data, only 52.1% of points fell within the EE1 envelope. This means that the current algorithm cannot qualify the accuracy defined by EE1. However, the uncertainties of this algorithm were in good agreement within EE2. Except for Dhaka_University, more than 66% of match-ups fell within the EE2 envelope. For the overall data, 69.2% of the overall data fell within the EE2, and the retrievals highly agreed with the AERONET measurements with an r-value of 0.922.

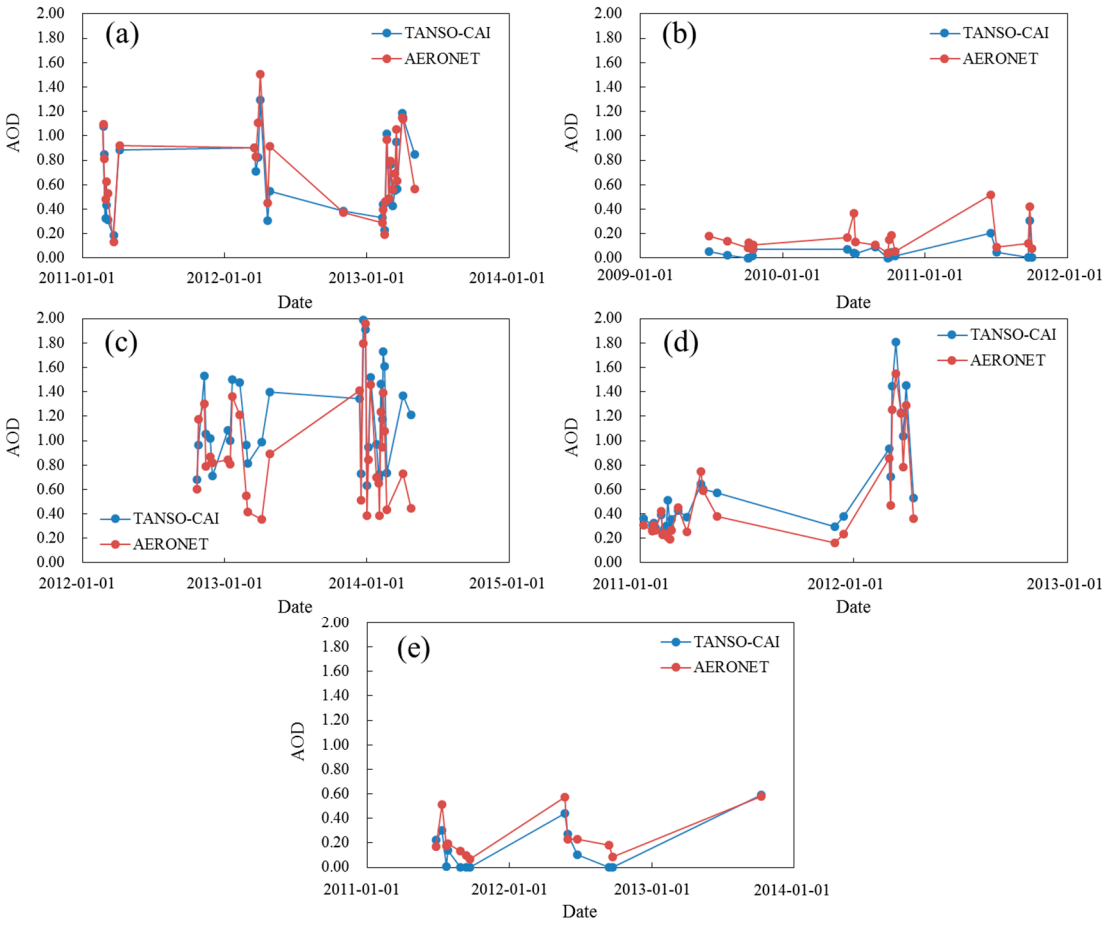

Figure 10. Variation curve of AODs from the spatially and temporally collocated TANSO-CAI and Aerosol Robotic Network (AERONET) data; (**a**) Vientiane site; (**b**) Xinglong site; (**c**) Dhaka_University site; (**d**) Chiang_Mai_Met_Sta site; and (**e**) Ussuriysk site.

Table 4. Geographical information and summary statistics for the entire data set and each individual site: longitude, latitude, elevation, number of samples (N), correlation coefficients (r), root mean square errors (RMSE), mean bias errors (MBE), and expected errors (EE).

Site Name	Longitude (Decimal Degrees)	Latitude (Decimal Degrees)	ELEVATION (Meters)	N	Mean AOD	r	RMSE	MBE	EE1	EE2
Vientiane	102.57	17.99	170	28	0.716	0.921	0.141	−0.059	78.6%	82.1%
Xinglong	117.58	40.40	970	19	0.164	0.791	0.136	−0.110	31.6%	73.7%
Dhaka_University	90.40	23.73	34	31	0.915	0.855	0.328	0.245	41.9%	51.6%
Chiang_Mai_Met_Sta	98.97	18.77	312	26	0.520	0.974	0.140	0.099	61.5%	73.1%
Ussuriysk	132.16	43.70	280	13	0.249	0.904	0.119	−0.089	38.5%	69.2%
Total				117	0.584	0.922	0.205	0.045	52.1%	69.2%

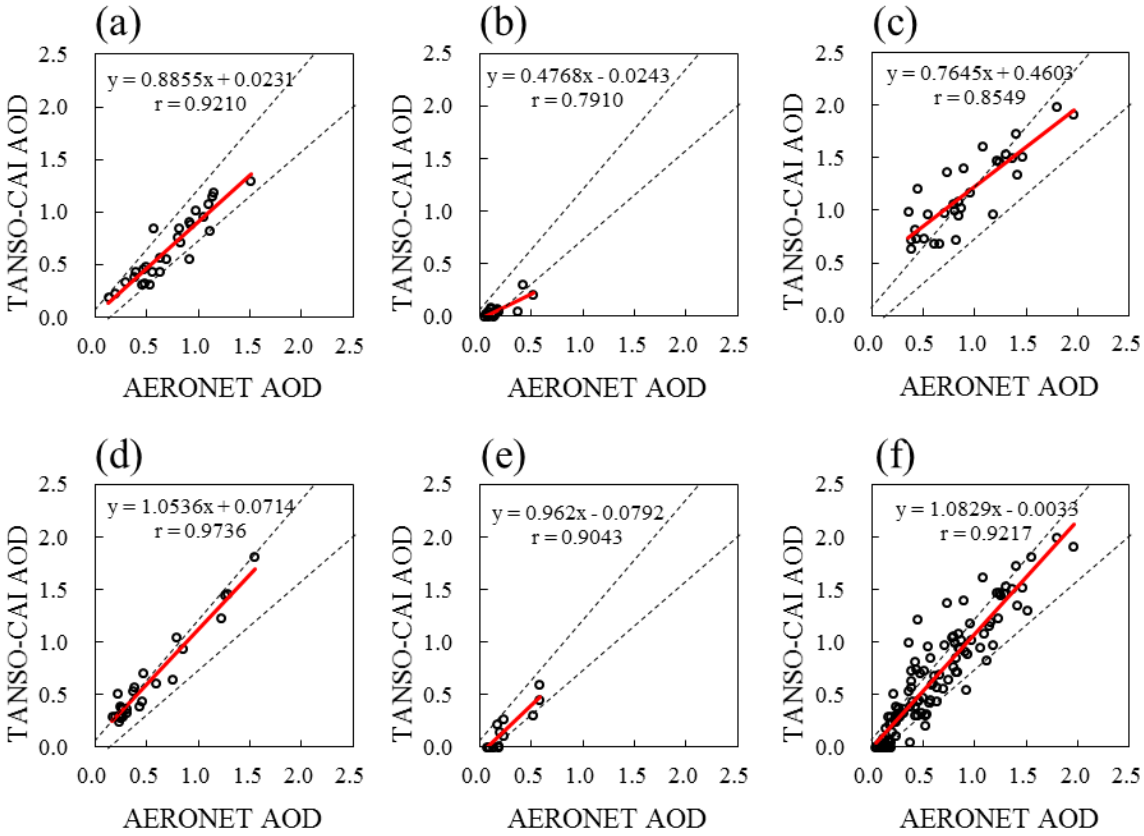

Figure 11. Validation of TANSO-CAI retrievals against AERONET measurements over different regions. (**a**) Vientiane site; (**b**) Xinglong site; (**c**) Dhaka_University site; (**d**) Chiang_Mai_Met_Sta site; (**e**) Ussuriysk site; and (**f**) for all sites. The red solid and dashed lines are the regression line and the expected error ($\pm$(0.1 + 15% $AOD_{AERONET}$)) envelope line, respectively.

As part of this algorithm was developed based on several studies using the MODIS DT algorithm, the retrievals made using our algorithm were also compared with the MODIS standard aerosol products. Here, a MODIS DT Collection 6 AOD product at 3 km (MYD04_3K) from Aqua with a similar overpass time to GOSAT was used. Figure 12 compares the TANSO-CAI and MODIS retrievals made at comparable times and areas. The comparison results (Figure 11) show that the current algorithm performs reasonably well overall and also for individual sites. The correlations of TANSO-CAI and MODIS AODs are very strong, and the statistical r-values are all higher than 0.87. MODIS has 36 channels, and the DT algorithm uses the blue (at 0.47 μm), red (at 0.65 μm), and SWIR (at 2.1 μm) channels to account for the surface signals. Moreover, several additional aerosol models were also defined and used in AOD retrievals. However, compared with MODIS, the limitations of

the TANSO-CAI spectral bands made aerosol retrieval very challenging. As GOSAT TANSO-CAI is not equipped with the 2.1 μm band, the estimation of the surface reflectance has to rely on the relationship of 1.6 vs. 2.1. Although this relationship has proven to be extremely robust under low aerosol conditions, the associated uncertainty may in fact serve to increase actual AOD retrieval. Additionally, as the MODIS DT is a multi-channel algorithm, the MODIS blue band is also employed in AOD retrieval. However, due to the lack of a blue band in TANSO-CAI, only one visible band is used for AOD retrieval. The single-band algorithm has no degree of freedom to select aerosol models [71].

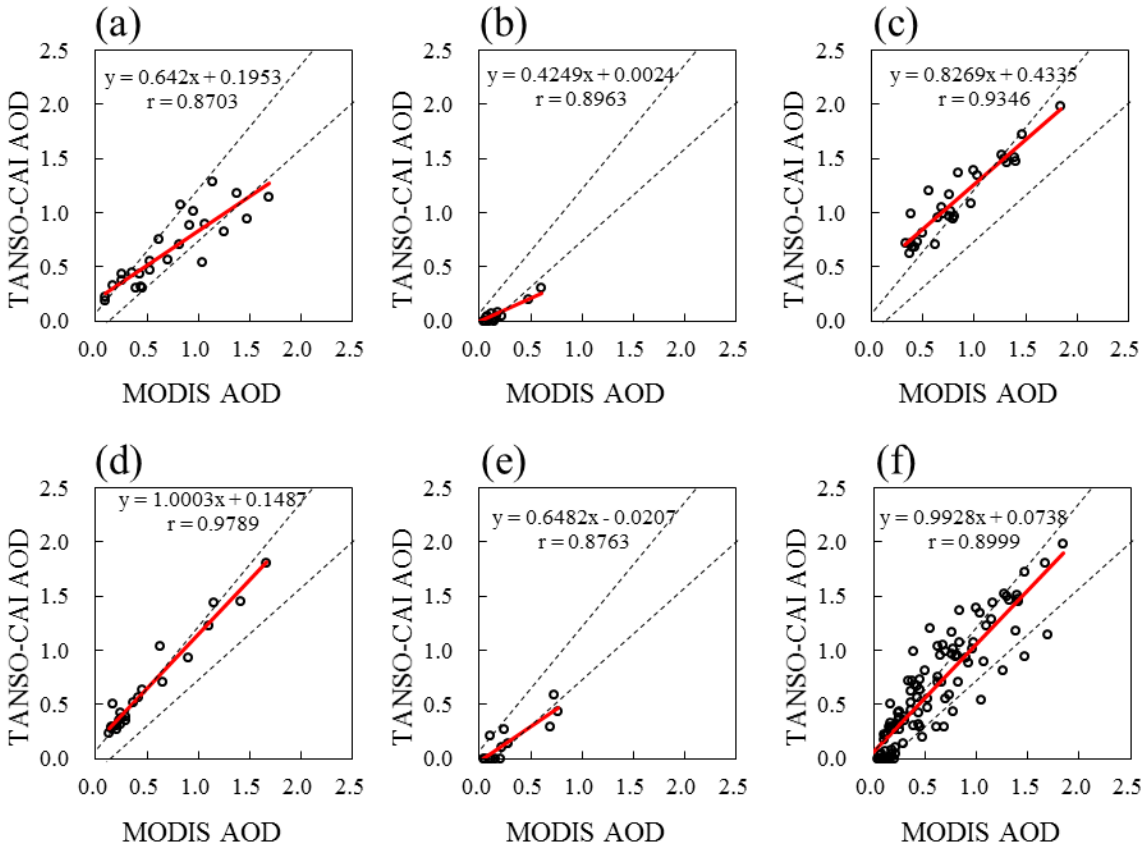

Figure 12. Comparison of TAOSN-CAI retrievals against MYD04_3K AOD over different regions. (**a**) Vientiane site; (**b**) Xinglong site; (**c**) Dhaka_University site; (**d**) Chiang_Mai_Met_Sta site; (**e**) Ussuriysk site; and (**f**) for all sites. The red solid and dashed lines are the regression line and the expected error ($\pm$(0.1 + 15% $AOD_{AERONET}$)) envelope line, respectively.

We used the 6S radiative transfer code to simulate the relationships between TOA and surface reflectance in the TANSO-CAI 0.67 μm band under five different aerosol models: continental, urban, biomass, desert, and maritime [72]. Figure 13a–d shows the simulation results for the different models when surface reflectances were 0.02, 0.04, 0.06, and 0.08, respectively. We can see that under the urban aerosol model, the relationship between TOA and surface reflectance differs greatly from those of other aerosol models. With the exception of the urban aerosol model, there are only slight differences between each of the models. This implied that for the TANSO-CAI 0.67 μm band-based algorithm, the continental aerosol model could potentially be used as the common assumption to describe aerosol scattering and absorption properties, but actually doing so would lead to large errors when the aerosol properties were in accordance with the urban aerosol type. Consequently, these deficiencies can restrict the performance of TANSO-CAI in its accuracy and range of application.

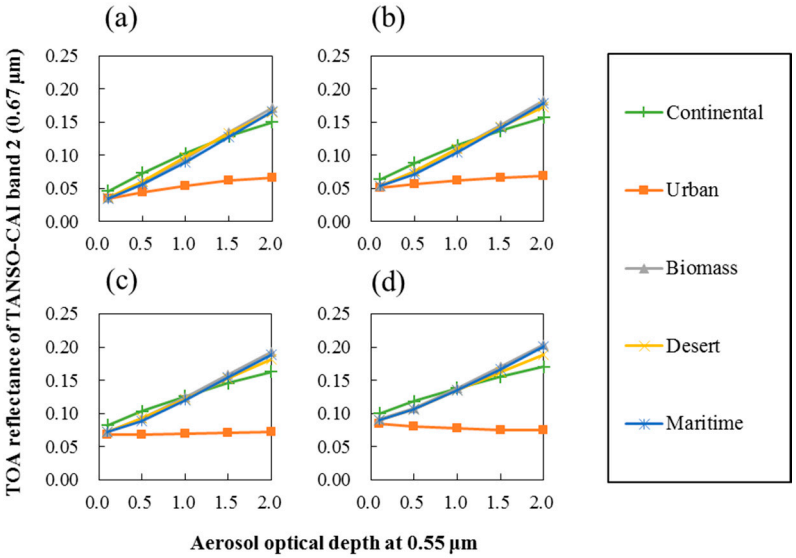

Figure 13. TANSO-CAI TOA reflectance as a function of AOD and surface reflectance at 0.67 μm under different aerosol models. The assumed surface reflectances are: (**a**) 0.02; (**b**) 0.04; (**c**) 0.06; and (**d**) 0.08. Simulation is performed under the observation geometric conditions with solar zenith angle = 30°, satellite zenith angle = 30°, and relative azimuth angles = 180°.

Expectedly, Greenhouse Gases Observing Satellite 2 (GOSAT-2), the successor to GOSAT which is scheduled for launch in the Japanese fiscal year 2017, will carry a new observation instrument: Cloud and Aerosol Imager 2 (CAI-2). CAI-2 will have greatly improved observation capabilities over CAI; 10 bands in the ultraviolet, visible, near infrared, and shortwave infrared region, and the capacity to observe in both the forward and backward directions (Table 5) [73]. Hence, the current algorithm could be adapted to operate on next-generation instruments, greatly ameliorating the existing problems caused by the single-band algorithm.

Table 5. Specification of GOSAT TANSO-CAI-2.

+20 deg. (Forward Viewing)			−20 deg. (Backward Viewing)		
Band Number	**Bandwidth (μm)**	**Spatial Resolution (m)**	**Band Number**	**Bandwidth (μm)**	**Spatial Resolution (m)**
1	0.333–0.353	460	6	0.370–0.390	460
2	0.433–0.453	460	7	0.540–0.560	460
3	0.664–0.684	460	8	0.664–0.684	460
4	0.859–0.879	460	9	0.859–0.879	460
5	1.585–1.675	920	10	1.585–1.675	920

5. Conclusions

In this study, we proposed a GOSAT TANSO-CAI adapted Dark Target algorithm for aerosol retrieval based on ideas from the MODIS DT algorithm. TANSO-CAI measures reflectance near the 1.6 μm wavelength. It does not measure the 2.1 μm wavelength. In the MODIS DT algorithm, relationships between the 2.1 μm and VIS (red and blue) bands are used to account for the surface signals. In order to take full advantage of these relationships in the TANSO-CAI retrieval algorithm, we analyzed the reflectance relationship between 1.6 μm and 2.1 μm with the help of a MODIS surface reflectance product, and found that their relationship varies according to the surface condition.

The vegetation index (NDVI or $AFRI_{2.1}$) can be a very accurate indicator of surface conditions, and the surface reflectance at 2.1 μm has been parameterized as an empirically derived function of the 1.6 μm surface reflectance and vegetation index. We grouped experimental data with given $AFRI_{2.1}$ values, and analyzed the changing characteristics of the regression functions (slope and intercept) obtained for the grouped data set. Our results show that the slopes of the regressions are extremely well correlated with $AFRI_{2.1}$, with an r-value of -0.968, and the relationship between regression intercepts and $AFRI_{2.1}$ is also high, with an r-value of -0.742. This means that the reflectance relationships at 1.6 μm and 2.1 μm are typically dependent on the amount of vegetation.

In terms of experimental results, an $AFRI_{2.1}$-based regression function for estimating reflectance at 2.1 μm from data observed at 1.6 μm was summarized. We tested and compared the performances in estimation with the linear regression function and the $AFRI_{2.1}$-based regression function. This comparison of results indicated that the $AFRI_{2.1}$-based method has much better performance, and shows higher agreement with the true values.

As the $AFRI_{2.1}$ is calculated using the reflectance of the NIR and 2.1 μm bands, and because TANSO-CAI does not possess the 2.1 μm band, it is very difficult to directly use this $AFRI_{2.1}$-based method in the application of TANSO-CAI. As such, we initially developed a method to estimate $AFRI_{2.1}$ using the NIR and 1.6 μm bands. Then, using the estimated $AFRI_{2.1}$, a reflectance connection between the 1.6 μm and VIS bands can be compiled via the estimated reflectance in the 2.1 μm band.

In the MODIS DT algorithm, the estimation of VIS surface reflectance is dependent on both geometry (scattering angle) and surface conditions ($NDVI_{SWIR}$). Our results show that $AFRI_{2.1}$ is highly correlated with the $NDVI_{SWIR}$ under low aerosol loading conditions (r-value of 0.943). Since both $NDVI_{SWIR}$ and $AFRI_{2.1}$ are defined by longer wavelengths that are much less influenced by aerosol than regular NDVI, similar to the MODIS DT algorithm, we took the scattering angle and $AFRI_{2.1}$ into account to develop a method for estimating surface reflectance at 0.67 μm from the 1.6 μm band for TANSO-CAI.

AOD retrieval over land from TANSO-CAI was conducted based on estimated surface reflectance. These retrievals were validated by comparison against measurements from five different AERONET sites. The retrievals displayed very high consistency with the AERONET measurements (r-value of 0.922). The uncertainty values for this algorithm were assessed using the expected error envelope of $\pm(0.1 + 15\%\ AOD_{AERONET})$, and 69.2% of retrievals fell within this expected error lines. The mean bias error for the overall experimental data is 0.045.

The demonstrated approaches for GOSAT TANSO-CAI AOD retrieval can be used in conjunction with other sensors that measure reflectance in corresponding wavelength bands, especially sensors which have SWIR bands near the 1.6 μm wavelength but lack the 2.1 μm band. This study offers a new idea for estimating surface reflectance in the VIS band from the SWIR band. However, like the MODIS DT algorithm, this algorithm is also unable to work over bright land surfaces. In addition, although the 1.6 μm and 2.1 μm SWIR bands are not sensitive to fine-mode aerosol particles, under the dust aerosol condition, the atmosphere is no longer transparent. Therefore, use of the current algorithm is restricted to dust aerosols [74,75].

With regard to the second-generation sensor GOSAT CAI-2, this work could be a meaningful reference, and the existing deficiencies (e.g., the single-band based retrieval method) caused by current instrument limitations can be expected to improve in the future. Red and blue bands are used in the current MODIS DT algorithm, and GOSAT CAI-2 will provide new measurement capability in the blue band. According to Equation (3), an approach for estimating surface reflectance in the blue band from the 1.6 μm band could be developed, one which has the potential to modify the current algorithm for GOSAT CAI-2 by employing the blue band. Moreover, both CAI and CAI-2 possess the ultraviolet band, and the AOD at the ultraviolet band is an important parameter. The use of the ultraviolet band would be helpful for detecting absorbing aerosol, and offers a good opportunity for further studies to take the advantage of the GOSAT CAI ultraviolet band in AOD retrieval.

Acknowledgments: This work was conducted with funding from the Joint Research Program of Arid Land Research Center, Tottori University (No. 27C2010), and the National Natural Science Foundation of China (41401478). We are thankful to the GOSAT teams of Japan for providing TANSO-CAI data. We are grateful to the AERONET teams at the stations used in this paper. We also thank the Level-1 and Atmosphere Archive and Distribution System (LAADS) and Land Processes Distributed Active Archive Center (LP DAAC) for providing MODIS Aerosol Products and MODIS Surface Reflectance Products.

Author Contributions: Xiufeng Wang and Guosheng Zhong conceived the study and all authors contributed to its design. Xiufeng Wang, Hiroshi Tani, Meng Guo, Anthony R. Chittenden, and Shinji Matsumura supervised and provided technical support to the research. Shuai Yin and Zhongyi Sun assisted with the satellite and ground-based data collection and processing. Guosheng Zhong performed the data analysis and wrote the paper.

Conflicts of Interest: The authors declare no conflict of interest.

References

1. Sun, L.; Wei, J.; Bilal, M.; Tian, X.; Jia, C.; Guo, Y.; Mi, X. Aerosol Optical Depth Retrieval over Bright Areas Using Landsat 8 OLI Images. *Remote Sens.* **2015**, *8*, 23. [CrossRef]
2. Choudhry, P.; Misra, A.; Tripathi, S. Study of MODIS derived AOD at three different locations in the Indo Gangetic Plain: Kanpur, Gandhi College and Nainital. *Ann. Geophys.* **2012**, *30*, 1479–1493. [CrossRef]
3. Mateos, D.; Anton, M.; Toledano, C.; Cachorro, V.; Alados-Arboledas, L.; Sorribas, M.; Costa, M.J.; Baldasano, J. Aerosol radiative effects in the ultraviolet, visible, and near-infrared spectral ranges using long-term aerosol data series over the Iberian Peninsula. *Atmos. Chem. Phys.* **2014**, *14*, 13497–13514. [CrossRef]
4. Jiang, X.; Liu, Y.; Yu, B.; Jiang, M. Comparison of MISR aerosol optical thickness with AERONET measurements in Beijing metropolitan area. *Remote Sens. Environ.* **2007**, *107*, 45–53. [CrossRef]
5. Zhang, H.; Hoff, R.; Kondragunta, S.; Laszlo, I.; Lyapustin, A. Aerosol optical depth (AOD) retrieval using simultaneous GOES-East and GOES-West reflected radiances over the western United States. *Atmos. Meas. Tech.* **2013**, *6*, 471–486. [CrossRef]
6. Riffler, M.; Popp, C.; Hauser, A.; Fontana, F.; Wunderle, S. Validation of a modified AVHRR aerosol optical depth retrieval algorithm over Central Europe. *Atmos. Meas. Tech.* **2010**, *3*, 1255–1270. [CrossRef]
7. Liu, Y.; Park, R.J.; Jacob, D.J.; Li, Q.; Kilaru, V.; Sarnat, J.A. Mapping annual mean ground-level PM2.5 concentrations using Multiangle Imaging Spectroradiometer aerosol optical thickness over the contiguous United States. *J. Geophys. Res. Atmos.* **2004**, *109*. [CrossRef]
8. NOAA Earth System Research Laboratory Global Monitoring Division Global Radiation Group. Available online: https://www.esrl.noaa.gov/gmd/grad/surfrad/aod/ (accessed on 8 January 2017).
9. Kaufman, Y.; Tanré, D.; Gordon, H.; Nakajima, T.; Lenoble, J.; Frouin, R.; Grassl, H.; Herman, B.; King, M.; Teillet, P. Passive remote sensing of tropospheric aerosol and atmospheric correction for the aerosol effect. *J. Geophys. Res. Atmos.* **1997**, *102*, 16815–16830. [CrossRef]
10. Kaufman, Y.; Tanré, D.; Remer, L.A.; Vermote, E.; Chu, A.; Holben, B. Operational remote sensing of tropospheric aerosol over land from EOS moderate resolution imaging spectroradiometer. *J. Geophys. Res. Atmos.* **1997**, *102*, 17051–17067. [CrossRef]
11. Kokhanovsky, A.; Breon, F.-M.; Cacciari, A.; Carboni, E.; Diner, D.; Di Nicolantonio, W.; Grainger, R.; Grey, W.; Höller, R.; Lee, K.-H. Aerosol remote sensing over land: A comparison of satellite retrievals using different algorithms and instruments. *Atmos. Res.* **2007**, *85*, 372–394. [CrossRef]
12. De Leeuw, G.; Holzer-Popp, T.; Bevan, S.; Davies, W.H.; Descloitres, J.; Grainger, R.G.; Griesfeller, J.; Heckel, A.; Kinne, S.; Klüser, L. Evaluation of seven European aerosol optical depth retrieval algorithms for climate analysis. *Remote Sens. Environ.* **2015**, *162*, 295–315. [CrossRef]
13. Kaufman, Y.J.; Wald, A.E.; Remer, L.A.; Gao, B.-C.; Li, R.-R.; Flynn, L. The MODIS 2.1-µm channel-correlation with visible reflectance for use in remote sensing of aerosol. *IEEE Trans. Geosci. Remote Sens.* **1997**, *35*, 1286–1298. [CrossRef]
14. Remer, L.A.; Kaufman, Y.; Tanré, D.; Mattoo, S.; Chu, D.; Martins, J.V.; Li, R.-R.; Ichoku, C.; Levy, R.; Kleidman, R. The MODIS aerosol algorithm, products, and validation. *J. Atmos. Sci.* **2005**, *62*, 947–973. [CrossRef]

15. Diner, D.J.; Martonchik, J.V.; Kahn, R.A.; Pinty, B.; Gobron, N.; Nelson, D.L.; Holben, B.N. Using angular and spectral shape similarity constraints to improve MISR aerosol and surface retrievals over land. *Remote Sens. Environ.* **2005**, *94*, 155–171. [CrossRef]
16. Grey, W.M.; North, P.R.; Los, S.O.; Mitchell, R.M. Aerosol optical depth and land surface reflectance from multiangle AATSR measurements: Global validation and intersensor comparisons. *IEEE Trans. Geosci. Remote Sens.* **2006**, *44*, 2184–2197. [CrossRef]
17. Deuzé, J.; Bréon, F.; Devaux, C.; Goloub, P.; Herman, M.; Lafrance, B.; Maignan, F.; Marchand, A.; Nadal, F.; Perry, G. Remote sensing of aerosols over land surfaces from POLDER-ADEOS-1 polarized measurements. *J. Geophys. Res. Atmos.* **2001**, *106*, 4913–4926. [CrossRef]
18. Levy, R.C.; Remer, L.A.; Mattoo, S.; Vermote, E.F.; Kaufman, Y.J. Second-generation operational algorithm: Retrieval of aerosol properties over land from inversion of Moderate Resolution Imaging Spectroradiometer spectral reflectance. *J. Geophys. Res. Atmos.* **2007**, *112*. [CrossRef]
19. Levy, R.; Mattoo, S.; Munchak, L.; Remer, L.; Sayer, A.; Patadia, F.; Hsu, N. The Collection 6 MODIS aerosol products over land and ocean. *Atmos. Meas. Tech.* **2013**, *6*, 2989–3034. [CrossRef]
20. Soufflet, V.; Tanré, D.; Royer, A.; O'Neil, N. Remote sensing of aerosols over boreal forest and lake water from AVHRR data. *Remote Sens. Environ.* **1997**, *60*, 22–34. [CrossRef]
21. Mei, L.; Xue, Y.; Kokhanovsky, A.; von Hoyningen-Huene, W.; de Leeuw, G.; Burrows, J. Retrieval of aerosol optical depth over land surfaces from AVHRR data. *Atmos. Meas. Tech. Discuss.* **2013**, *6*, 2227–2251. [CrossRef]
22. Holzer-Popp, T.; Schroedter-Homscheidt, M.; Breitkreuz, H.; Martynenko, D.; Klüser, L. Improvements of synergetic aerosol retrieval for ENVISAT. *Atmos. Chem. Phys.* **2008**, *8*, 7651–7672. [CrossRef]
23. Xie, D.; Cheng, T.; Zhang, W.; Yu, J.; Li, X.; Gong, H. Aerosol type over east Asian retrieval using total and polarized remote sensing. *J. Quant. Spectrosc. Radiat. Transf.* **2013**, *129*, 15–30. [CrossRef]
24. Levy, R.; Munchak, L.; Mattoo, S.; Patadia, F.; Remer, L.; Holz, R. Towards a long-term global aerosol optical depth record: Applying a consistent aerosol retrieval algorithm to MODIS and VIIRS-observed reflectance. *Atmos. Meas. Tech.* **2015**, *8*, 4083–4110. [CrossRef]
25. Dark Target (MODIS Aerosol Retrieval Algorithm), About the Algorithm. Available online: https://darktarget.gsfc.nasa.gov/algorithm (accessed on 26 December 2016).
26. Dark Target (MODIS Aerosol Retrieval Algorithm). Available online: http://darktarget.gsfc.nasa.gov/content/what-difference-between-dark-target-and-deep-blue (accessed on 28 December 2016).
27. Hsu, N.; Jeong, M.J.; Bettenhausen, C.; Sayer, A.; Hansell, R.; Seftor, C.; Huang, J.; Tsay, S.C. Enhanced deep blue aerosol retrieval algorithm: The second generation. *J. Geophys. Res. Atmos.* **2013**, *118*, 9296–9315. [CrossRef]
28. Dark Target (MODIS Aerosol Retrieval Algorithm), Platforms, VIIRS. Available online: https://darktarget.gsfc.nasa.gov/platforms/viirs (accessed on 26 December 2016).
29. Fukuda, S.; Nakajima, T.; Takenaka, H.; Higurashi, A.; Kikuchi, N.; Nakajima, T.Y.; Ishida, H. New approaches to removing cloud shadows and evaluating the 380 nm surface reflectance for improved aerosol optical thickness retrievals from the GOSAT/TANSO-Cloud and Aerosol Imager. *J. Geophys. Res.: Atmos.* **2013**, *118*, 13520–13531. [CrossRef]
30. Greenhouse Gases Observing SATellite Project. Available online: http://www.gosat.nies.go.jp/eng/GOSAT_pamphlet_en.pdf (accessed on 26 December 2016).
31. Gao, L.; Li, J.; Chen, L.; Zhang, L.; Heidinger, A.K. Retrieval and validation of atmospheric aerosol optical depth from AVHRR over China. *IEEE Trans. Geosci. Remote Sens.* **2016**, *54*, 6280–6291. [CrossRef]
32. Algorithm Theoretical Basis Document (ATBD) for CO_2 and CH_4 Columun Amounts Retrieval from GOSAT TANSO-FTS SWIR. Available online: http://data.gosat.nies.go.jp/GosatUserInterfaceGateway/guig/doc/documents/ATBD_FTSSWIRL2_V1.1_en.pdf (accessed on 26 December 2016).
33. Jung, Y.; Kim, J.; Kim, W.; Boesch, H.; Lee, H.; Cho, C.; Goo, T.-Y. Impact of aerosol property on the accuracy of a CO_2 retrieval algorithm from satellite remote sensing. *Remote Sens.* **2016**, *8*, 322. [CrossRef]
34. Sun, L.; Sun, C.; Liu, Q.; Zhong, B. Aerosol optical depth retrieval by HJ-1/CCD supported by MODIS surface reflectance data. *Sci. China Earth Sci.* **2010**, *53*, 74–80. [CrossRef]
35. Istomina, L.; von Hoyningen-Huene, W.; Kokhanovsky, A.; Schultz, E.; Burrows, J. Remote sensing of aerosols over snow using infrared AATSR observations. *Atmos. Meas. Tech.* **2011**, *4*, 1133–1145. [CrossRef]

36. Zhang, Y.; Li, Z.; Qie, L.; Zhang, Y.; Liu, Z.; Chen, X.; Hou, W.; Li, K.; Li, D.; Xu, H. Retrieval of Aerosol Fine-Mode Fraction from Intensity and Polarization Measurements by PARASOL over East Asia. *Remote Sens.* **2016**, *8*, 417. [CrossRef]
37. Hou, P.; Jiang, W.; Cao, G.; Li, J. Aerosol retrieval with satellite image and correlation analyses between aerosol distribution and urban underlaying surface. *Int. J. Remote Sens.* **2012**, *33*, 3232–3251. [CrossRef]
38. Remer, L.A.; Wald, A.E.; Kaufman, Y.J. Angular and seasonal variation of spectral surface reflectance ratios: Implications for the remote sensing of aerosol over land. *IEEE Trans. Geosci. Remote Sens.* **2001**, *39*, 275–283. [CrossRef]
39. Gatebe, C.K.; King, M.D.; Tsay, S.-C.; Ji, Q.; Arnold, G.T.; Li, J.Y. Sensitivity of off-nadir zenith angles to correlation between visible and near-infrared reflectance for use in remote sensing of aerosol over land. *IEEE Trans. Geosci. Remote Sens.* **2001**, *39*, 805–819. [CrossRef]
40. Lyapustin, A.I. Three-dimensional effects in the remote sensing of surface albedo. *IEEE Trans. Geosci. Remote Sens.* **2001**, *39*, 254–263. [CrossRef]
41. Algorithm Theoretical Basis Document for TANSO-CAI L1B Processing. Available online: https://data.gosat.nies.go.jp/GosatWebDds/productorder/distribution/user/ATBD_CAIL1B_V1.0_en.pdf (accessed on 22 December 2016).
42. Algorithm Theoretical Basis Document for TANSO-CAI L1B+ Processing. Available online: https://data.gosat.nies.go.jp/GosatWebDds/productorder/distribution/user/ATBD_CAIL1BP_V1.01_en.pdf (accessed on 23 December 2016).
43. NIES GOSAT Product Format Descriptions. Available online: https://data.gosat.nies.go.jp/GosatWebDds/productorder/distribution/user/GOSAT_ProductDescription_V1.50_en.pdf (accessed on 24 December 2016).
44. Vermote, E.F.; Kotchenova, R.; Ray, J. MODIS Surface Reflectance User's Guide. Version 1.3. MODIS Land Surface Reflectance Science Computing Facility. Available online: http:modis-sr.ltdri.org/products/MOD09_UserGuide_v1_3.pdf (accessed on 28 October 2016).
45. Modis Land Surface Reflectance Science Computing Facility Homepage. Available online: https://modis-sr.ltdri.org/index.html (accessed on 25 December 2016).
46. Wang, S.; Yang, M.; Li, J.; Shen, Q.; Zhang, F. MODIS surface reflectance product (MOD09) validation for typical inland waters in China. In Proceedings of the SPIE Ocean Remote Sensing and Monitoring from Space, Beijing, China, 13 October 2014; International Society for Optics and Photonics: Bellingham, WA, USA, 2014. [CrossRef]
47. Fan, L.; Berger, F.H.; Liu, H.; Bernhofer, C. Validating MODIS land surface reflectance products using ground-measured reflectance spectra—A case study in semi-arid grassland in Inner Mongolia, China. *Int. J. Remote Sens.* **2014**, *35*, 1715–1728. [CrossRef]
48. Vermote, E.F.; Kotchenova, S. MODIS Meetings—MODIS Land Collection 5 Workshop Presentations. Available online: https://modis.gsfc.nasa.gov/sci_team/meetings/c5meeting/pres/day1/vermote.pdf (accessed on 28 October 2016).
49. Holben, B.N.; Eck, T.; Slutsker, I.; Tanre, D.; Buis, J.; Setzer, A.; Vermote, E.; Reagan, J.; Kaufman, Y.; Nakajima, T. AERONET—A Federated Instrument Network and Data Archive for Aerosol Characterization. *Remote Sens. Environ.* **1998**, *66*, 1–16. [CrossRef]
50. Slutsker, I.; Kinne, S. Wavelength dependence of the optical depth of biomass burning, urban, and desert dust aerosols. *J. Geophys. Res.* **1999**, *104*, 31333–31349.
51. Ångström, A. The parameters of atmospheric turbidity. *Tellus* **1964**, *16*, 64–75. [CrossRef]
52. Vermote, E.; El Saleous, N.; Justice, C.; Kaufman, Y.; Privette, J.; Remer, L.; Roger, J.; Tanre, D. Atmospheric correction of visible to middle-infrared EOS-MODIS data over land surfaces: Background, operational algorithm and validation. *J. Geophys. Res. Atmos.* **1997**, *102*, 17131–17141. [CrossRef]
53. Modis Land Surface Reflectance Science Computing Facility, Validation. Available online: http://modis-sr.ltdri.org/pages/validation.html (accessed on 21 December 2016).
54. Zhong, G.; Wang, X.; Tani, H.; Guo, M.; Chittenden, A.; Yin, S.; Sun, Z.; Matsumura, S. A modified aerosol free vegetation index algorithm for aerosol optical depth retrieval using GOSAT TANSO-CAI data. *Remote Sens.* **2016**, *8*, 998. [CrossRef]
55. Rouse, J., Jr. *Monitoring the Vernal Advancement and Retrogradation (Green Wave Effect) of Natural Vegetation*; Technical Report; NASA: Washington, DC, USA, 1974.

56. NASA Earth Observatory. Available online: http://earthobservatory.nasa.gov/Features/MeasuringVegetation/measuring_vegetation_2.php (accessed on 28 October 2016).
57. Dark Target (MODIS Aerosol Retrieval Algorithm), Land Surface Reflectance. Available online: https://darktarget.gsfc.nasa.gov/algorithm/land/surface-reflectance (accessed on 25 December 2016).
58. Karnieli, A.; Kaufman, Y.J.; Remer, L.; Wald, A. AFRI—Aerosol Free Vegetation Index. *Remote Sens. Environ.* **2001**, *77*, 10–21. [CrossRef]
59. Liu, G.-R.; Liang, C.-K.; Kuo, T.-H.; Lin, T.-H.; Huang, S. Comparison of the NDVI, ARVI and AFRI vegetation index, along with their relations with the AOD using SPOT 4 vegetation data. *Terr. Atmos. Ocean. Sci.* **2004**, *15*, 15–32. [CrossRef]
60. Ben-Ze'ev, E.; Karnieli, A.; Agam, N.; Kaufman, Y.; Holben, B. Assessing vegetation condition in the presence of biomass burning smoke by applying the Aerosol-Free Vegetation Index (AFRI) on MODIS images. *Int. J. Remote Sens.* **2006**, *27*, 3203–3221. [CrossRef]
61. Levy, R.C.; Remer, L.A.; Munchak, L.A. A surface reflectance scheme for retrieving aerosol optical depth over urban surfaces in MODIS dark target retrieval algorithm. *Atmos. Meas. Tech.* **2016**, *9*, 3293–3308.
62. Vermote, E.F.; Tanré, D.; Deuze, J.L.; Herman, M.; Morcette, J.-J. Second simulation of the satellite signal in the solar spectrum, 6S: An overview. *IEEE Trans. Geosci. Remote Sens.* **1997**, *35*, 675–686. [CrossRef]
63. Vermote, E.F.; Kotchenova, S. Atmospheric correction for the monitoring of land surfaces. *J. Geophys. Res. Atmos.* **2008**, *113*. [CrossRef]
64. Vermote, E.F.; El Saleous, N.Z.; Justice, C.O. Atmospheric correction of MODIS data in the visible to middle infrared: First results. *Remote Sens. Environ.* **2002**, *83*, 97–111. [CrossRef]
65. Le Treut, H. Greenhouse gases, aerosols and reducing future climate uncertainties. *Surv. Geophys.* **2012**, *33*, 723–731. [CrossRef]
66. EUMETSAT Surface Albedo Validation Sites. Available online: http://savs.eumetsat.int (accessed on 18 October 2016).
67. Xie, Y.; Zhang, Y.; Xiong, X.; Qu, J.J.; Che, H. Validation of MODIS aerosol optical depth product over China using CARSNET measurements. *Atmos. Environ.* **2011**, *45*, 5970–5978. [CrossRef]
68. Nichol, J.E.; Bilal, M. Validation of MODIS 3 km Resolution Aerosol Optical Depth Retrievals over Asia. *Remote Sens.* **2016**, *8*, 328. [CrossRef]
69. Levy, R.C.; Remer, L.A.; Kleidman, R.G.; Mattoo, S.; Ichoku, C.; Kahn, R.; Eck, T. Global evaluation of the Collection 5 MODIS dark-target aerosol products over land. *Atmos. Chem. Phys.* **2010**, *10*, 10399–10420. [CrossRef]
70. Dark Target (MODIS Aerosol Retrieval Algorithm), Validation Results. Available online: https://darktarget.gsfc.nasa.gov/validation/results (accessed on 26 December 2016).
71. Zhang, H.; Lyapustin, A.; Wang, Y.; Kondragunta, S.; Laszlo, I.; Ciren, P.; Hoff, R. A multi-angle aerosol optical depth retrieval algorithm for geostationary satellite data over the United States. *Atmos. Chem. Phys.* **2011**, *11*, 11977–11991. [CrossRef]
72. Vermote, E.; Tanré, D.; Deuzé, J.; Herman, M.; Morcrette, J.; Kotchenova, S. Second Simulation of a Satellite Signal in the Solar Spectrum-Vector (6SV). Available online: http://6s.ltdri.org/files/tutorial/6S_Manual_Part_1.pdf (accessed on 28 December 2016).
73. GOSAT-2, about GOSAT-2, Spacecraft & Instruments. Available online: http://www.gosat-2.nies.go.jp/about/spacecraft_and_instruments/ (accessed on 29 December 2016).
74. Kaufman, Y.J.; Tanré, D.; Boucher, O. A satellite view of aerosols in the climate system. *Nature* **2002**, *419*, 215–223. [CrossRef] [PubMed]
75. Wang, J.; Xu, X.; Spurr, R.; Wang, Y.; Drury, E. Improved algorithm for MODIS satellite retrievals of aerosol optical thickness over land in dusty atmosphere: Implications for air quality monitoring in China. *Remote Sens. Environ.* **2010**, *114*, 2575–2583. [CrossRef]